Tweezing and Manipulating Nanomaterials on Tapered Optical Fiber to Develop Surface-Enhanced Raman Spectroscopy (SERS) Substrate

By Navneet Kaur

A dissertation submitted to the Faculty of Graduate Studies

Lakehead University

In partial fulfillment of the requirements for the degree of

Master of Science

Physics

Department of Physics

Lakehead University

2020

ABSTRACT

A compact and cost-effective fiber-based probe was manufactured for the detection of chemicals at low concentrations using Surface-Enhanced Raman Spectroscopy (SERS). Multi-mode optical fiber was tapered with a dynamic etching process using Hydrofluoric (HF) acid. The desired length, tip diameter, and cone angle of the tapered fiber were obtained by using this process. The SERS substrate was prepared by depositing Gold Nanorods (GNRs) on the tapered fiber surface by the phenomenon called Optical Tweezing (OT). The tapered fiber was characterized by using a Scanning Electron Microscope (SEM) and Optical Microscope. Light from a a He-Ne laser was coupled to the untapered end of the tapered fiber to study the distribution of GNRs using the Optical Microscope. The effect of different tweezing wavelengths, and the tapered length on the distribution of GNRs on the tapered fiber surface was investigated. It was observed that the maximum surface area of tapered fiber was covered with GNRs when tweezed consecutively with two different wavelengths (1064 nm and 632 nm). The application of the tapered fiber covered with GNRs as a SERS substrate was investigated for a chemical and material, Rhodamine 6G (R6G) and Graphite, respectively. Furthermore, we presented the tweezing of an another compound Zn $(OH)_2$ on the tapered fiber surface when mixed with GNRs solution using two lasers consecutively.

Contributions

1. **N. Kaur,** et al., "Tweezing and manipulating the distribution of gold nanorods (GNRs) on a tapered optical fiber to develop plasmonic **s**tructure", OSA Continuum,Vol.3, Issue 9, pp. 2415-2422 (2020).

2. **N. Kaur,** et al., "Tweezing Zn $(OH)_2$ on the surface of the tapered fiber" – Manuscript under Preparation.

Conferences

1. **N. Kaur,** et al., "Fiber-based Nanoprobe for the Detection of Chemicals" CAP Conference, Simon Fraser University, Burnaby, BC, 3 – 7 June 2019.

Acknowledgement

I would like to take this opportunity to thank my supervisor, Dr. Gautam Das. I would not have been able to complete this research without his support and guidance. I am thankful to the Lakehead University Physics Department for giving me a chance to pursue my studies here. I want to give a special thanks to my supervisory committee members Dr. Apichart Linhananta and Dr. Mark Gallagher. I would like to thank all the members of the Photonic Research Group for their immense support and especially Joshua Trevisanutto. I would also like to thank Dr. Guosheng Wu for providing me with SEM training. Additionally, I would like to thank Dr. Alla Reznik and her research group member Oleksandr Grynko for giving us access to the Reinshaw Raman system to perform experiments. I am thankful to my family and friends, whose invaluable encouragement supported me throughout my studies at Lakehead University.

This thesis is dedicated to my mother, Parminder Kaur,

my father, Avtar Singh,

and my brother, Arshdeep Singh.

Contents

List of Figures

List of Tables

Chapter 1

Introduction

1.1 Optical Fiber

An optical fiber is a cylindrical dielectric waveguide that is designed to operate at optical frequencies [1]. K.C Kao first proposed the concept of optical fiber in 1966 [2]. Figure 1 below shows the structure of the optical fiber. The core of the fiber has a higher refractive index (n_1) compared to the cladding (n_2), and the light transmitted along the fiber core follows "Total Internal Reflection" (TIR).

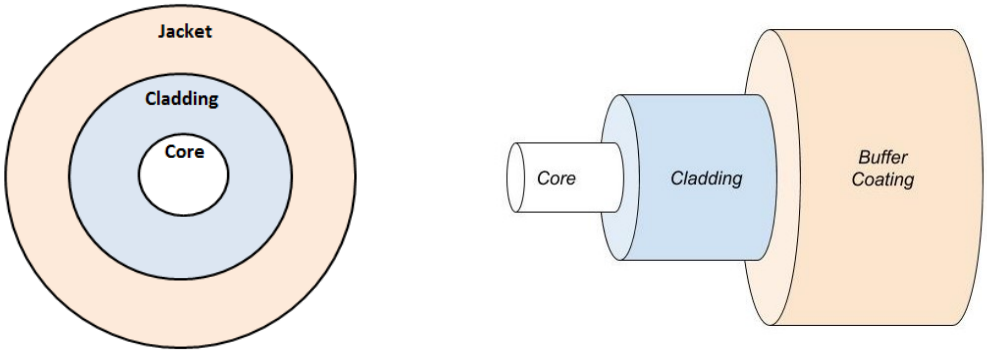

Figure 1.1: (a) Schematic diagram of a fiber showing the cross-sectional view with core, cladding and outer coating (Jacket), (b) 3D view of a fiber.

The core material is generally glass, which is surrounded by a glass cladding. The outer layer, known as the jacket or buffer coating, adds strength to make the fiber stronger and more durable. Light launched into the optical fiber, which satisfies the total internal reflection condition at the core-cladding interface, remains confined in the core and propagates along the optical fiber's length.

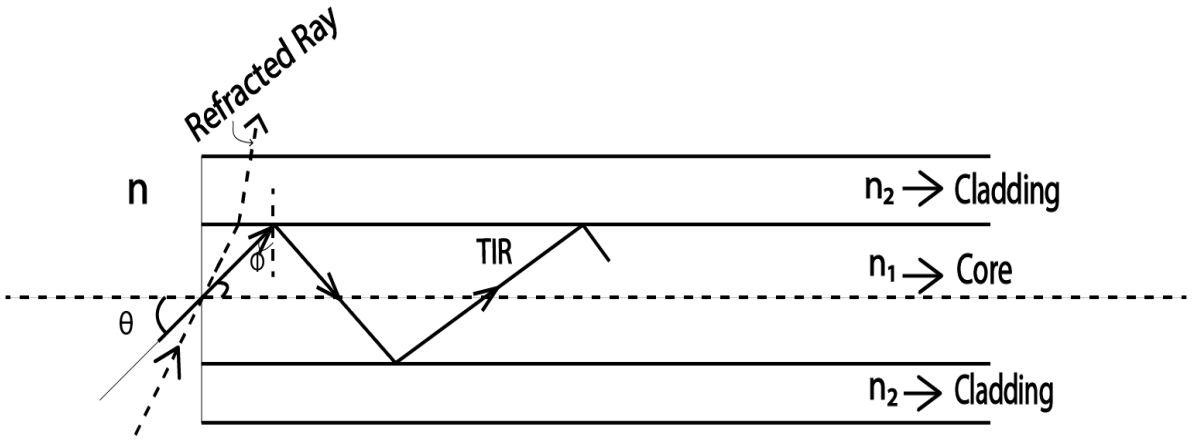

Figure 1.2: Light propagation along an optical fiber [1].

Light rays incident on the core of the fiber from a medium with refractive index, n, at an angle θ, which is less than equal to the acceptance angle and hits the core-cladding interface at an angle φ, will follow the total internal reflection. One can obtain the critical angle (φ_c) of incidence at the core-cladding interface to support total internal reflection [1]:

$$Sin(\varphi_c) = \frac{n_2}{n_1} \qquad (1)$$

The maximum incident angle, or the acceptance angle, θ_{max} is [1]:

$$n\ Sin\ \theta_{max} = NA = (n_1 - n_2)^{\frac{1}{2}} \quad (2)$$

The parameter NA is called Numerical Aperture, which defines the light gathering capability of the optical fiber.

The material used to manufacture an optical fiber can be either polymer or glass. Silica (SiO_2) glass is most commonly used to prepare the core of the fiber. The refractive index of the glass is approximately 1.46. To either increase or decrease the index of refraction of the glass core, it can be doped with GeO_2 or B_2O_3, respectively [1].

Based on the number of modes supported, an optical fiber can be categorized into two types:

1. Multimode fiber (MMF)
2. Single-mode fiber (SMF)

Multimode fiber (MMF) is useful for short-distance communication systems. The core diameter of MMF ranges from 50 – 200 μm approximately, as shown in figure 1.3 (a). On the other hand, Single-mode fiber (SMF) is better for long-distance communication systems, and the core diameter of SMF ranges from 8 – 12 μm approximately, as shown in figure 1.3 (b) [1]. The cladding diameter for both MMF and SMF is 125 μm (Figure 1.3).

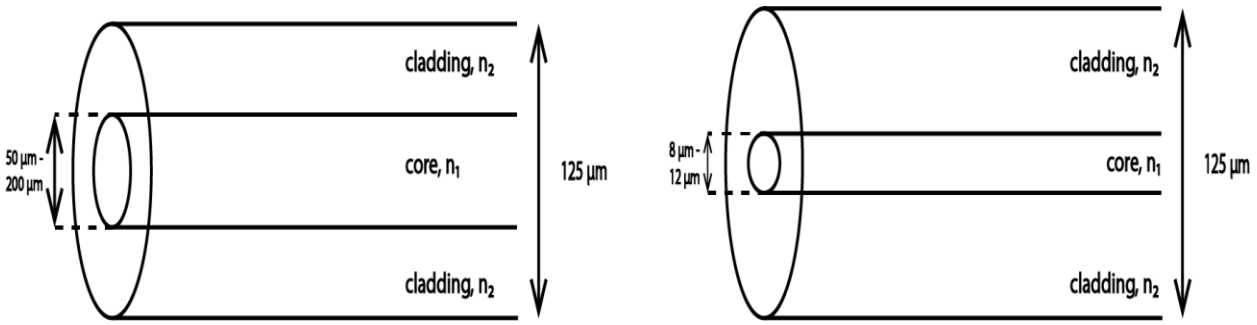

Figure 1.3: Diagrams illustrating the (a) MMF, and (b) SMF [1].

Single-mode fiber (SMF) is used in communication, and multimode fiber has applications in sensing [1]. Passive optical devices based on optical fiber can be used as sensors to measure pressure, strain and temperature in harsh environments. Sensors based on optical fiber are cost-effective, compact, and highly sensitive [3].

1.2 Tapered Fiber

Tapered fiber can be manufactured by various methods, such as heating-pulling, polishing and chemical etching of optical fiber [4-6]. Tapered optical fiber has many applications, including: developing SERS (Surface-Enhanced Raman Spectroscopy) substrates [7;8], glucose sensing [9], non-linear optics [10], and in trapping yeast cells [11]. Tapered optical fiber has an advantage as the evanescent field can interact with the external medium [12]. As the diameter of the core decreases, the power starts leaking outside the core along with the tapered length, and the surrounding medium (air, water, etc.) act as cladding [13].

In this research, the tapered shape of an optical fiber was obtained using a dynamic etching process. The schematic of a tapered fiber is shown in figure 1.4. The structure of a tapered fiber shows how the radius of the fiber changes with its length [14]. We used the dynamic etching process, where 1.5 ml of Hydrofluoric (HF) acid of 50% concentration was used to etch the fiber. The length of the tapered region was such that the core of the fiber was exposed to the outer (surrounding) medium, which acts as cladding for the tapered fiber [7].

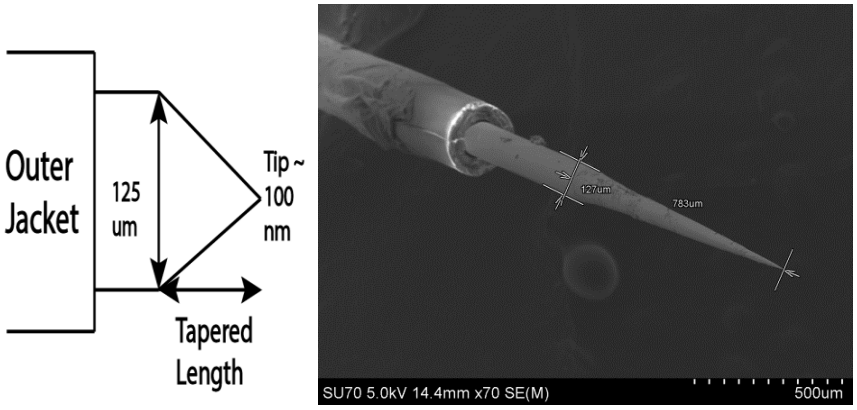

(a) **(b)**

Figure 1.4: (a) Schematic illustration, and (b) SEM image of a tapered optical fiber labelled with the length of the tapered fiber along with the outer jacket, cladding diameter.

The process of tapering an optical fiber followed several steps. Firstly, before immersing the fiber in the Hydrofluoric (HF) acid solution, the outer jacket (layer) of the fiber was removed using a stripper and cleaned with ethanol to remove the debris. The second step was to cleave the fiber with the help of a fiber cleaver and then studied the fiber under a microscope to ensure the

quality of the cleaved end, which should be flat. Finally, the fiber was mounted on a translation stage to immerse in the Hydrofluoric acid. The fiber was withdrawn at a certain speed, which gave the desired tapered length and cone-angle [7]. The length of the tapered fiber varies with the withdrawal speed, and results for this are discussed later in Chapter 2. Also, during the etching process, it is necessary to cover the HF solution with an organic solvent (e.g. isooctane) to stop the evaporation of HF at room temperature [8]. In addition to that, the organic solvent keeps the HF volume constant. Finally, the characteristics of the tapered fiber (e.g., length and tip diameter) were examined using a Scanning Electron Microscope (SEM).

1.3 Weakly Guiding Approximation

To acquire more specific understanding of the power propagation mechanism in an optical fiber, it is important to study Maxwell's equations. The four Maxwell's equations are as follows [1]:

$$\nabla \mathrm{x} \mathrm{E} = -\frac{\partial B}{\partial t} \tag{3}$$

$$\nabla \mathrm{x} \mathrm{H} = \frac{\partial D}{\partial t} \tag{4}$$

$$\nabla \cdot \mathrm{D} = 0 \tag{5}$$

$$\nabla \cdot \mathrm{B} = 0 \tag{6}$$

where D = εE and B = μH, where ε is permittivity, and μ is the permeability of the medium. We can combine Maxwell's equations to obtain the wave equation. One needs to solve the wave equation to get the optical fiber's characteristic parameters such as the number of modes, mode

field distributions and mode field diameter, which is a complex process. Though the weakly guiding approximation can be used when the difference in refractive indices of the core and cladding is small, i.e., $\Delta << 1$, where $\Delta = (n_1^2 - n_2^2)/2n_2^2$. Under this condition, the vector wave equation reduces to a scalar wave equation [1]. In the weakly guiding approximation, the transverse component of the electric field is much higher than the longitudinal component and modes are known as "Linearly Polarized" and represented by LP_{vm}.

1.4 Modes in Cylindrical Waveguide

The number of modes propagating along the fiber depends on the V-number, which is a dimensionless quantity [1]:

$$V = 2\pi a \frac{(n_1 - n_2)^{\frac{1}{2}}}{\lambda} \quad (7)$$

where a = core radius,

n_1 = core refractive index,

n_2 = cladding refractive index,

λ = wavelength

Under the weakly guiding approximation when the difference in refractive indices of the core and cladding is very small, i.e., less than 1%, an optical fiber with $V < 2.405$ supports only the fundamental mode $LP_{01,}$ and the fiber is known as Single-Mode. For a tapered fiber in a sensing application, the core is surrounded by an external medium, and the index difference is very high. Therefore the weakly guiding approximation is not applicable. Figure 1.5 shows the fundamental

mode field distribution of the HE_{11} mode supported by the tapered fiber. The refractive indices of the core and cladding were 1.46, and 1.33, respectively. The mode field distribution was obtained by solving vector wave equations [14;15].

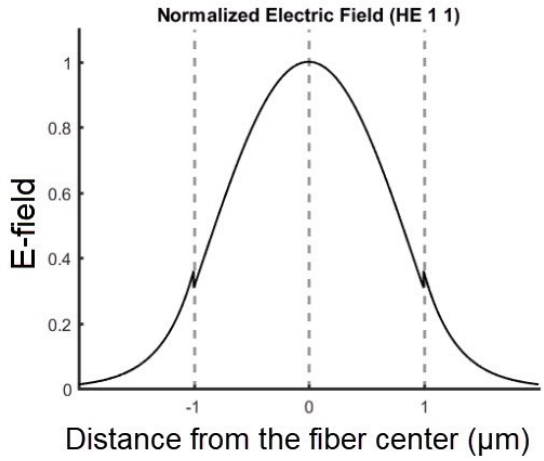

Figure 1.5: Electric field distribution of HE_{11} mode in the core and cladding [15].

In the experiment, the laser light was coupled at the untapered end of the tapered fiber and propagated along the tapered length to the tip of tapered fiber. As the diameter of the fiber decreases, the number of modes supported by the fiber also decreases. The field in the cladding, known as the evanescent field, interacts with the surrounding medium. Further, the surrounding medium behaves as the cladding, and it should have a lower refractive index than the core to fulfill the TIR conditions. We have estimated the number of modes supported by the tapered fiber at particular locations (diameter) on the tapered fiber by modifying the MATLAB codes available from the MATLAB Optical Fiber Toolbox [15]. Figure 1.6 shows the number of modes supported by a tapered fiber at three locations along the length calculated by using the modified program.

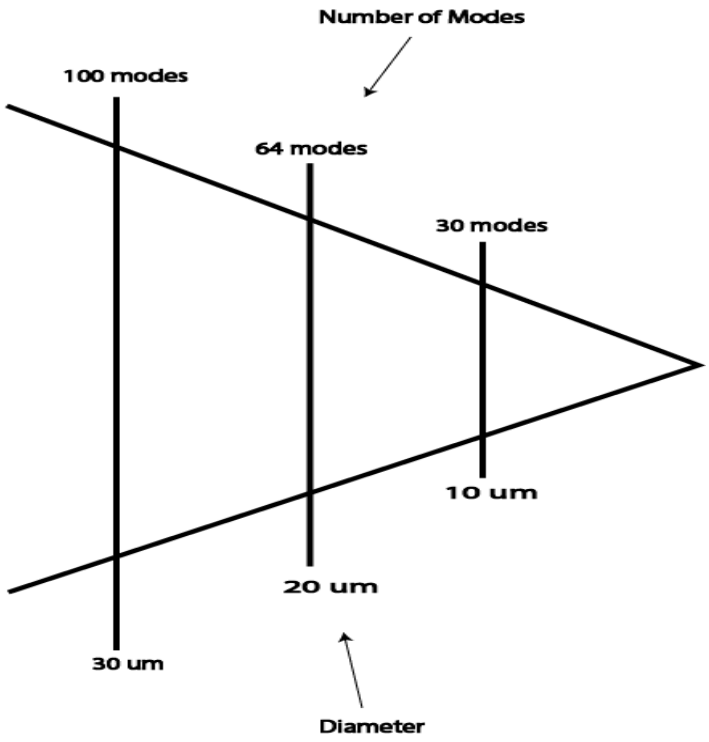

Figure 1.6: Diagram representing the section of a tapered fiber showing the number of modes corresponding to the diameters.

An important point to note here is that if the incident angle of light at the untapered end changed, the number of modes excited at a specific diameter also changes. Optimum coupling is required to excite all modes supported by the fiber at a particular diameter. The fraction of incident power in a mode depends on the total power launched into the fiber, and interference between them in the surrounding medium is also affected. The losses in the fiber can be due to misalignment and bending.

1.5 Mode Field Diameter

The mode field diameter (MFD) is an important characteristic parameter, which assists one in calculating coupling efficiency and dispersion in a single-mode optical fiber. This parameter can be calculated using the mode field distribution of the fundamental mode, where solving a vector wave equation is required. Under the weakly guiding approximation, one can use a Gaussian function (Figure 1.7) to estimate the MFD of the fundamental mode [14].

$$E(r) = E_0 \exp\left(\frac{-r^2}{W_0^2}\right) \quad (8)$$

Where r is the radial distance, E_0 is the field at r = 0, W_0 is the mode field radius, E(r) is the field of the fundamental mode (LP_{01}) mode.

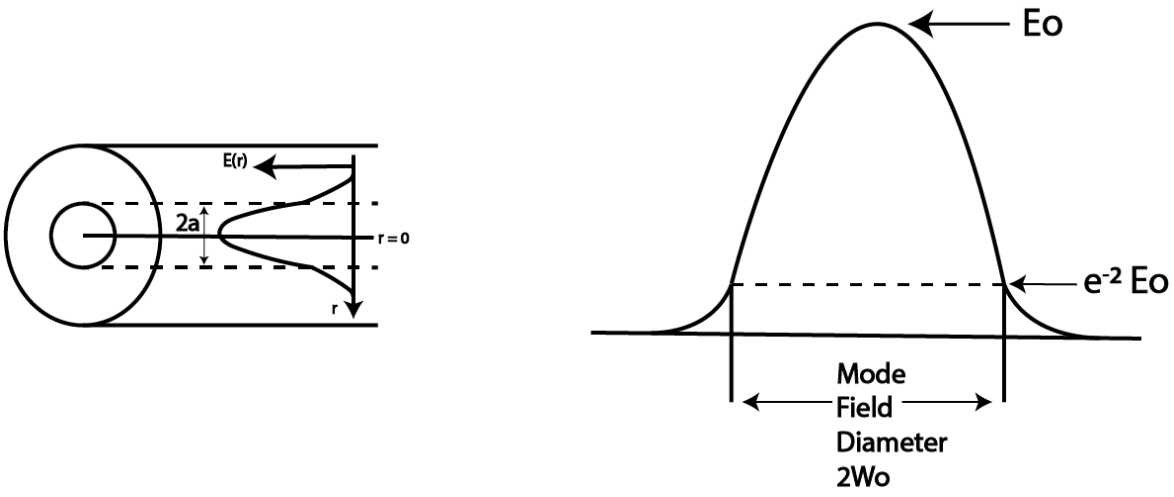

Figure 1.7: (a) Light distribution in a single-mode fiber (SMF); and (b) definition of mode field diameter (MFD) from Gaussian distribution.

1.6 Optical Tweezing (OT)

In 2018, Arthur Ashkin received a Nobel Prize for the discovery of trapping of dielectric particles using a single laser beam and the phenomenon is known as Optical tweezing [16]. In the experiment, a spatially filtered argon-laser (512.5 nm) was focused by a microscope objective with a high numerical aperture (NA =1.25). The laser beam was used to trap a cell present in the water solution. A microscope was used to see the trapped cells. The experiment also reported the photo of a 10 μm glass sphere trapped in water by using fluorescence to represent the path of the incident and scattering light beams. In the experiment, the dielectric particle size was in the range of 25 nm to 10 μm, and the particles were placed in a water solution.

Further, in 1978, A. Ashkin proposed the stable trapping and manipulation of atoms by resonance radiation pressure [17]. In the experiment, two highly intense laser beams from opposite directions were focused on the atomic particles, which form a trap. To develop optical tweezers (OTs), it became a powerful tool in physics as well as in biology. Using a focused laser beam, also known as laser tweezers, metallic nanoparticles can be trapped and accelerated using the forces by radiation pressure. The trapping of dielectric particle was explained using Ray optics where transfer of momentum from refracted light gave rise to the gradient and scattering forces. These two forces contributes in the trapping of either a dielectric particle or a metallic particle. In case of metallic particles, the incident electric field induces the dipole moment which cause particle to rotate or move. Thus, considering the case of plane wave, optical forces disintegrated into two components, gradient and scattering force [18].

An optical trap for the manipulation of biological particles, for example, viruses and bacteria, was reported by A. Ashkin *et al*. using Infrared (IR) light [19]. For the trap formation, a 1.06 μm Nd: YAG (neodymium-doped yttrium aluminum garnet) laser was coupled to the water-immersed microscope objective (NA = 1.25) connected with a focused lens and two beam splitters. The sample cell is placed between the microscope objective and condensed lens (CL), which was illuminated by a light source to provide a high-resolution view. This system has applications in the development of a single beam trap for particles of various sizes and shapes. The significant advantage of using the laser trap with IR light is that it causes less damage to the living cell. Due to the damage-free trapping, the reproduction of Escherichia coli (E. coli) and yeast cells were observed [19]. These techniques are proficient in manipulating cells, viruses, bacteria etc. in microbiology.

Optical tweezing has been observed to trap nanoparticles or nanomaterials on the surface of a tapered fiber, which has an application as a SERS substrate [20]. An evanescent wave was used to trap the nanoparticles, and the layer of nanoparticles was coated on the fiber with a thickness of 200 nm, which was confirmed by using a Scanning Electron Microscope (SEM). In another article, a double-tapered fiber (DTF) coated with gold nanoparticles was preferred for SERS applications over a flat end fiber (FTB) and a single tapered fiber (STF) since the DTF gives greater sensitivity of 10^{-9} M and more light collection efficiency. In the experiment, the results were compared to the Rhodamine 6G (R6G) [21].

In this tweezing phenomenon, a focused laser beam interacts with metallic particles, and they experience two forces [22]:

(1) Gradient force

(2) Scattering force

for stable trapping and to obtain optical tweezing, the magnitude of the gradient force should be greater than that of the scattering force, which is in the direction of propagation of light [22]. The gradient force arises when the electric field of incident light interacts with the induced dipoles in the particle. However, the technique of tweezing metallic nanoparticles is new and gives opportunities to develop a new plasmonic structure for research in nanophotonics [18]. The question is how to trap metallic particles with the same techniques as used in the trapping of dielectric particles. The metal surface reflects the incident light and produces large radiation pressure, but the reflected light from the metallic surface does not produce a gradient force as it does in the case of the dielectric particle [23]. It has already been established that metallic nanomaterials can be trapped on a fiber surface [7;20]. In 1994, K. Svoboda *et al.* experimentally demonstrated that the gradient force is the major component of the optical force, which is responsible for trapping metallic and dielectric particles. The condition for the successful trapping of metallic particles is that the size of the particle should be smaller than the incident wavelength. Moreover, the magnitude of gradient force depends on the intensity and polarizability of the particle, whereas the scattering force depends on beam intensity and the square of the polarizability [23].

Using the following expressions of optical forces, i.e. gradient and scattering forces [equations (9) and (10)] [24]:

$$F_g = \frac{1}{4}\mathrm{Re}(\alpha)\nabla|\varepsilon|^2 \qquad (9)$$

where, α = electric polarizability of the particle,

ε = complex amplitude of the electric field.

$$F_s = \sigma_{ext} \frac{n_2}{c} S \qquad (10)$$

where, σ_{ext} = extinction cross-section of the Rayleigh particle,

S = Poynting vector,

and n_2 = refractive index of the outer medium.

We calculated the magnitude of both the gradient and scattering forces for the modes LP_{01} and LP_{11} in the range of 2.17 µm - 4.17 µm diameter of the tapered fiber, using the modified program of MATLAB toolbox [15]. The particle radius was 0.010 µm, and the refractive index was 0.27 (Re) for a spherical Gold particle. The outside medium refractive index was taken as 1.33 (considered water solution). Figures 1.8 and 1.9 show the estimated magnitudes of gradient and scattering force for LP_{01} (HE_{11}) and LP_{11} (HE_{21}), respectively.

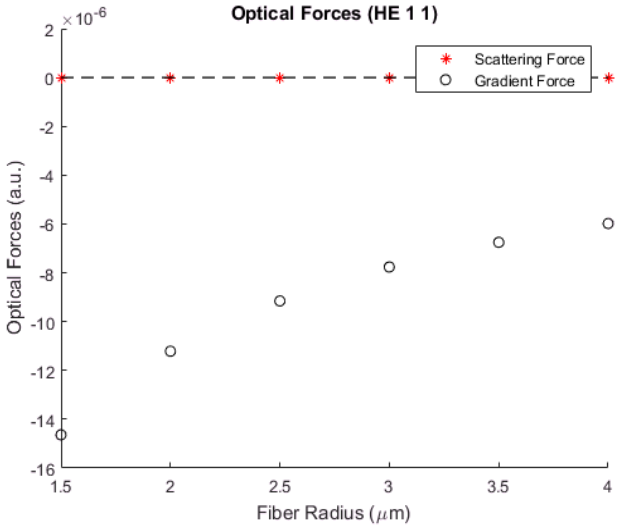

Figure 1.8: The calculated magnitude of optical forces for the fundamental mode HE_{11}.

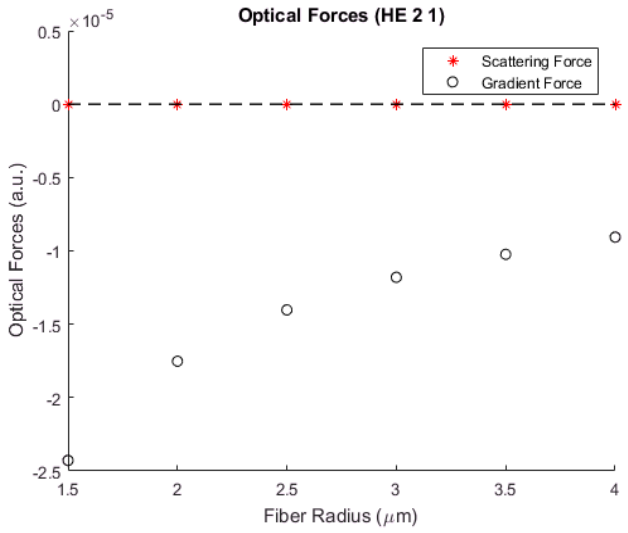

Figure 1.9: The calculated magnitude of optical forces for mode HE_{21}.

The laser wavelength used for simulations was 1064 nm. It is important to note that we used GNRs in our experiments instead of gold nanoparticles.

1.7 Gold Nanorods

Noble metallic nanoparticles, whose dimensions are smaller than the electron's mean free path, have dielectric constants that are different from the bulk metal. Additionally, they have unique optical properties that are dependent on the shape and size of the particles [25]. The applications of shape-dependent metal nanoparticles as a catalyst has been studied [26]. The different shape of the metallic nanoparticle yields a different Localized Surface Plasmon Resonance frequency (LSPR) [27]. The condition of LSPR occurs when the incident

electromagnetic wave and the conduction electrons in a metal oscillate in resonance [28]. In the bulk metals, the free electron density is responsible for the plasma frequency. In figure 1.10, it is clearly shown that free electrons are oscillating at a frequency as determined by the incident electromagnetic wave.

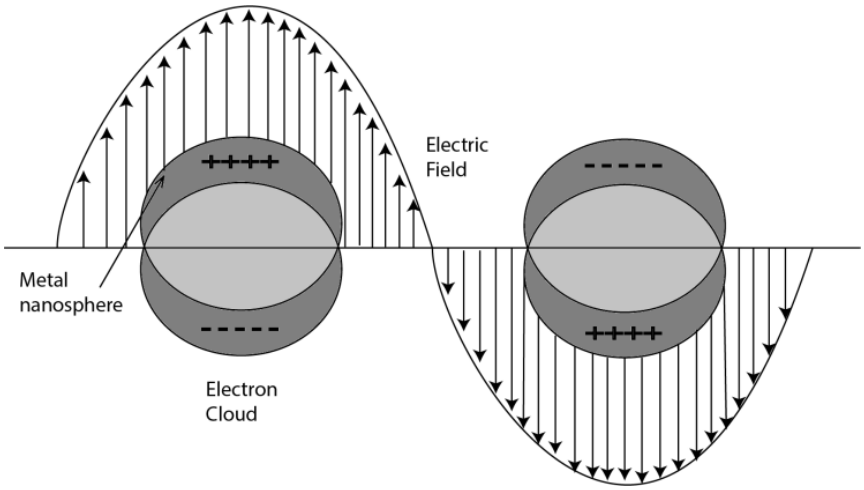

Figure 1.10: Image illustrating the localized surface plasmon of a metallic nanosphere.

Figure 1.10 shows how the electric field from the incoming light wave is creating a dipole in the metallic nanosphere by separating the charges within the particle. The dipole is aligned according to the electric field direction, and to attain resonance condition, the frequencies of incident light and dipole oscillation must be the same. This resonance condition leads to the more absorption and thus enhancement of the electric field. As the LSPR induces field enhancement, it has been investigated as the source of enhancement seen in Surface-Enhanced Raman

Spectroscopy (SERS) [27;28]. SERS was first used to obtain the Raman spectra of pyridine by adsorbing it on a silver electrode [29]. Moreover, V. Duyne *et al.* were successful in achieving the exceptional sensitivity of Raman spectroscopy for the pyridine adsorbed on the silver (Ag) substrate [30]. Overall, the SPR leads to an enhanced electric field near the metal layer and provides a base to study the light-matter interactions.

Due to the symmetric shape of the nanosphere, it has a single LSPR wavelength, which was observed around 520 nm wavelength when the diameter of the spherical particle was 20 nm [31]. The electric field enhancement factor around gold nanoparticles of various radii was theoretically examined when excited by the light matching different LSPR frequencies [32]. But in the present report, GNRs were being used to develop a SERS substrate on an optical fiber surface. The use of GNRs is more advantageous because the anisotropic shape of GNRs allows two localized plasmon resonance frequencies [33]. The dimensions of GNRs used to develop the SERS substrate were of length = 64 nm and diameter = 10 nm with the aspect ratio = length/diameter = 6.4. Because of the shape of GNRs, the two resonance frequencies were transverse (along the diameter) and longitudinal (along the length) of the nanorod, and the corresponding wavelengths were 532 nm and 1064 nm, respectively as shown in figure 1.11 [33]. These two LSPRs can be excited by two different laser wavelengths.

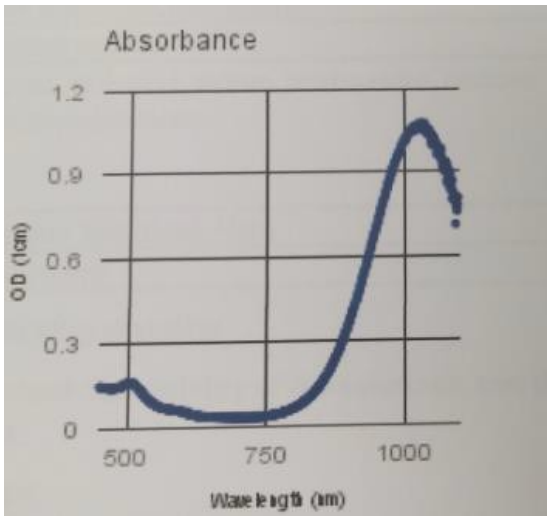

Figure 1.11: Absorption spectra for 64 nm length and 10 nm diameter GNRs, and the peaks are corresponding to their laser wavelengths [Nanopartz].

The longitudinal LSPR was stronger as the electron oscillation is along the longest axis (along the length of the nanorod). In contrast, the transverse LSPR was weaker because of the electron oscillations along the short axis (along the diameter of the nanorod) [33]. Further, the most significant enhancement was obtained in the Raman signal when GNRs were excited at the longitudinal excitation wavelength [34]. An important point to discuss is what happens when the aspect ratio of the GNR is changed. In an experiment performed with three different aspect ratios, i.e. 2.75, 3.1 and 3.31, it was observed that an increase in the aspect ratio of GNR leads to a shift in the longitudinal LSPR towards a higher wavelength (redshift).

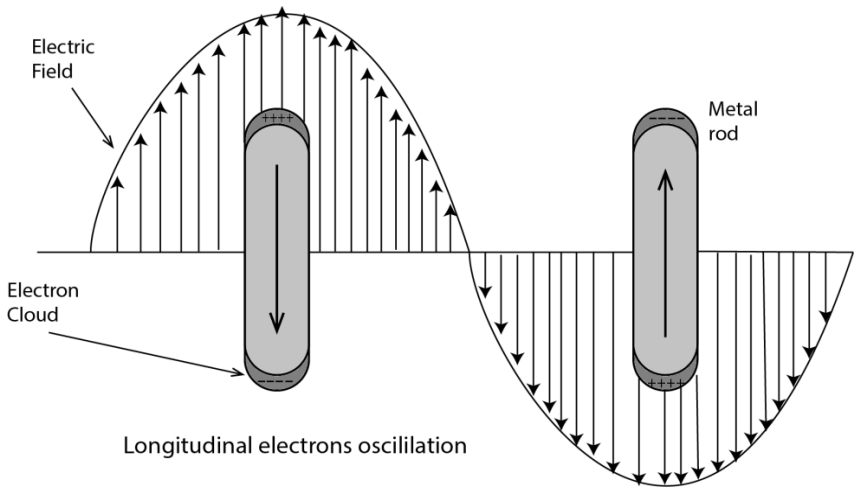

Figure 1.12: Illustration of localized surface plasmon resonance of a gold nanorod along the longitudinal direction.

In contrast, the transverse LSPR shows a slight change towards shorter wavelengths (blue shift) [31]. Another interesting point was that the colloidal solution of GNRs showed a variation in colour even when there was a small change in the aspect ratio [35].

In figure 1.12, the interaction of the electric field of incoming light and the metallic nanorod is being observed, which represents the longitudinal LSPR excitation in GNRs. The synthesis of GNRs can be done using various methods, and the major techniques are the template method, electrochemical method and seeded growth method. In the seeded growth method, the synthesis begins with the seed (i.e. gold nanosphere) as an initial step. Under the action of a surfactant [Cetyl trimethylammonium bromide (CTAB)], the seed grows into a GNR with a specific aspect ratio under certain conditions [36]. In 2001, Jana et al. first proposed the seeding growth method for large scale synthesis of GNRs [37]. The high-resolution TEM images (Figure 1.13) of the

GNRs with aspect ratio = 6.4 used in our research show the alignment and different facets of the GNRs.

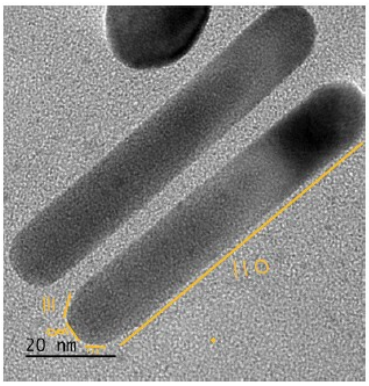

Figure 1.13: TEM image of GNR showing orientation along [110] direction.

In Reference [36], figure 4.1 show a TEM image of the Face Centered Cubic (FCC) structure of the GNR along the [110] direction and shows that the growth occurs along the [001] direction. Figure 1.13 is a replication of the above results from reference [36]. The properties of other metallic nanoparticles with different shapes have been studied, such as triangular silver (Ag) nanoparticles. Triangular Ag nanoparticles (also called Nano triangles) can be used in biological and chemical sensing for the detection of a Picomolar analyte [38]. Other morphologies of the nanoparticle include Nano stars, which can be used as a SERS substrate [39]. The synthesis and applications of various morphologies such as Nanowires, Nanoshells and Nano flowers have been discussed in detail [40-42].

The interaction of monochromatic light with a material produces elastically and in-elastically scattered photons. The Rayleigh scattering refers to the elastically scattered photons, and Raman scattering (stokes and anti-stokes) refers to the inelastically scattered photons. Raman and Krishnan first proposed the concept of elastically and in-elastically scattered photons in 1928 [43]. In figure 1.14, the energy level diagram represents the Rayleigh, stokes and anti-stokes scattering.

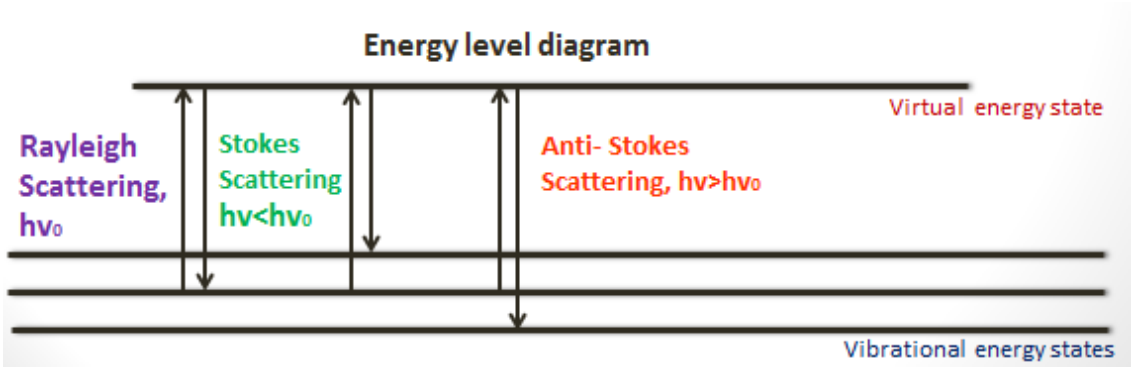

Figure 1.14: Energy level diagram representing 3 conditions: stokes (when energy is lost from the photon), anti-stokes (when the photon gains energy), and Rayleigh scattering (no gain or loss in energy by photon), where hv_0 is the incident photon energy, and hv is resultant energy.

Raman signal is weak in general, and to enhance the intensity of the Raman signal, a roughened metallic substrate was used, and first reported in 1974 when a Raman signal of pyridine adsorbed on an Ag surface was significantly enhanced [29]. The process is called Surface-Enhanced Raman Scattering (SERS), and the substrate is known as a SERS substrate.

Coinage metals such as Au, Ag, Cu are used to prepare SERS substrates as they produce strong surface plasmon resonances (SPR) [44]. In Raman spectroscopy, the number of in-elastically scattered photons are very low, and SERS drastically increases the Raman signal with an enhancement factor of approximately 10^{10}, and has been capable of observing a single molecule and proves the high sensitivity of the SERS technique [45]. SERS has been successfully used in the detection of an explosive in both solution and vapour form to the femtomolar (10^{-15}) and nanomolar (10^{-9}) range [46], rapid detection of environmental pollutants such as pesticides, heavy metal ions and pathogens [47]. In healthcare, SERS contributes to the accurate and early diagnosis of disease using silver nanoparticle (AgNP) based Nanosensors [48]. Another implementation of SERS is in the food industry, as food safety is a primary concern. Tetracycline (TET) is a contamination in milk, which affects the health of an individual, and 2 µl of milk sample was tested on a AgNPs based sensor. The concentration of TET in milk was measured using a Raman Spectrometer. The SERS substrate developed was cost-effective, and 100% recyclable [49]. In this thesis, the SERS substrate was prepared on the tapered fiber surface with gold nanorods (GNRs), and enhancement can be seen for the chemical and material such as Rhodamine 6G (R6G) and Graphite, respectively. The optical fibre-based sensor, also known as an optrodes, can be widely used for the detection of an analyte in liquids and to determine the contamination of water [50]. In a recent publication by Wang J. *et al.*, emphasis was given to the importance of an optical fiber-based SERS substrates as they are reliable, cost-effective, quick and efficient to detect toxic materials at low concentrations [51]. A plethora of reasons were presented to show the significance of Raman Spectroscopy as a powerful optical technique.

1.8 Organization of the Thesis

Chapter 1 gave an introduction to the optical fiber characteristics, advantages of tapered optical fiber, and phenomena such as Optical Tweezing, LSPR, and SERS. A description of the propagation of light in the fiber and modes has been discussed.

Chapter 2 describes the preparation of tapered fibers of different lengths using a dynamic etching process, and presents the results of tweezing of GNRs on the tapered fiber surface using single and double tweezing, and also presents the variation in GNRs distribution with the different length of the tapered fiber.

Chapter 3 reports the application of the tapered fiber plasmonic structure developed using single wavelength tweezing to detect the chemical and material such as R6G and Graphite, respectively at very low concentrations.

Chapter 4 describes the tweezing of other metal in the form of a chemical compound such as $Zn(OH)_2$ on the tapered fiber surface, and future work.

Chapter 2

Manipulation of GNRs distribution on the tapered fiber surface using Optical tweezing

2.1 Introduction

The applications of the cylindrical optical fiber were discussed in various fields, such as communications and sensing [1]. The etched cylindrical fiber known as tapered optical fiber has various advantages in sensing, and also cells can be trapped at the fiber surface using a focused laser beam [9;11]. In the tapered fiber, the core tapers down to a nanometer tip, and laser power escapes as the diameter of the fiber decreases. Thus, the outer medium starts behaving as the cladding, which allows the interaction between evanescent field waves and the external medium (GNRs solution) [12]. As a result, the GNRs can be trapped along the tapered fiber surface, and for successful tweezing, the magnitude of gradient force should be greater than the scattering force [22]. In Chapter 1, it was discussed that metallic nanoparticles of different shapes and sizes have unique optical properties [25;26]. The reason behind choosing GNRs for this application is because of the two Localized Surface Plasmon Resonance (LSPR) frequencies [35]. Raman Spectroscopy is a powerful technique and has been applied in numerous fields such as the

detection of explosives [46], environmental pollutants [47], early disease diagnosis [48] and the food industry [49] etc. In the experiments performed, we present the results from both single and double tweezing conditions. Also, the GNR distribution along the fiber surface was explored using either single or multiple tweezing. In this report, a Surface-Enhanced Raman Spectroscopy (SERS) substrate was prepared to enhance the Raman signal for the detection of R6G and Graphite.

2.2 Manufacturing Tapered Fiber

There are several techniques demonstrated to manufacture a tapered fiber [4-6]. As discussed in Chapter 1, chemical etching is one of the methods used to obtain tapered optical fiber using Hydrofluoric acid (∽ 50% concentration) [7]. The tapered fiber was manufactured by using a multimode fiber with a core and cladding diameter of 110 μm and 125 μm, respectively.

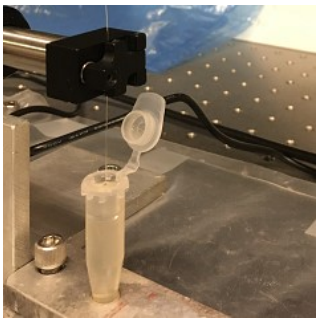

Figure 2.1: Experimental setup showing the etching process of a MMF using HF acid.

Figure 2.1 shows the experimental setup to manufacture the tapered fiber. The fiber holder was connected to a computer-controlled (ThorLabs, APT Software) translation stage, which facilitated control of the withdrawal speed of the fiber from the HF acid in the vial. A layer of

organic solvent isooctane was used on the top of the HF acid to prevent evaporation [8]. The ThorLabs APT software controlled the speed, acceleration and the position of the fiber. The desired length and diameter of the tapered fiber was obtained by changing the speed and the position of the fiber in the HF acid, Table 2.1 shows the experimental results performed by immersing the optical fiber in the HF acid and then being withdrawn at different speeds. Figure 2.2 shows the linear trend between the length of the tapered fiber vs speed of the translational stage.

speed (µm/s)	**length (µm)**
0.68	1710
0.58	1500
0.48	1210
0.38	1050
0.28	804
0.18	531

Table 2.1: Table representing the data of different tapered fiber lengths when withdrawn at different speeds.

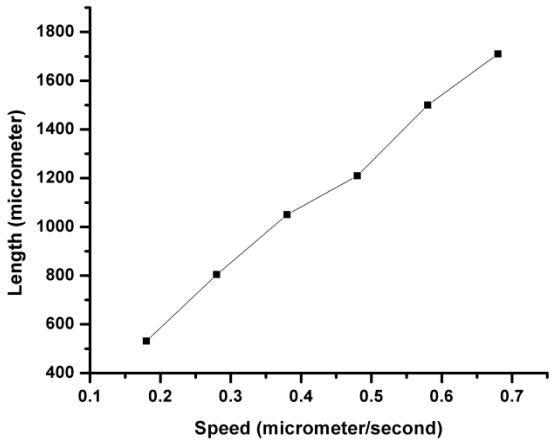

Figure 2.2: Graph representing the length of the tapered fiber vs the withdrawal speed of the fiber.

Figure 2.3 shows the tapered fiber of length 1.69 mm and a tip diameter 329 nm obtained at a speed of 0.68 µm/s. When manufacturing the plasmonic structure using GNRs, the length of the tapered fiber used was 1.69 mm.

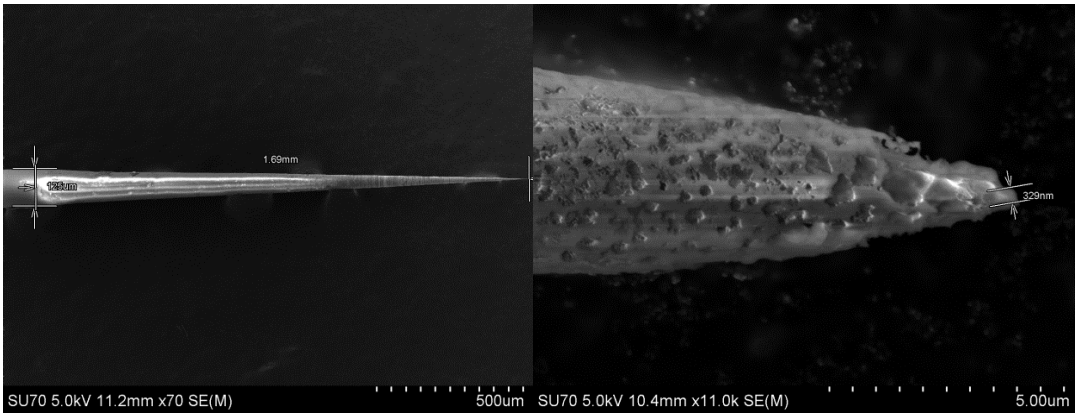

Figure 2.3: SEM images showing the length and a tip diameter of a tapered fiber etched at speed 0.68 µm/s.

After the etching process, the next step was tweezing the GNRs onto the tapered fiber. Figure 2.4 shows the experimental setup for tweezing. The laser light was coupled to the

untapered flat end of the fiber, and the tapered end was then dipped in the GNR solution. The tapered fiber was held by a fiber holder, which was mounted on the manual one-dimensional translational stage. The tapered end of the fiber was lowered into the GNR solution using the translation stage.

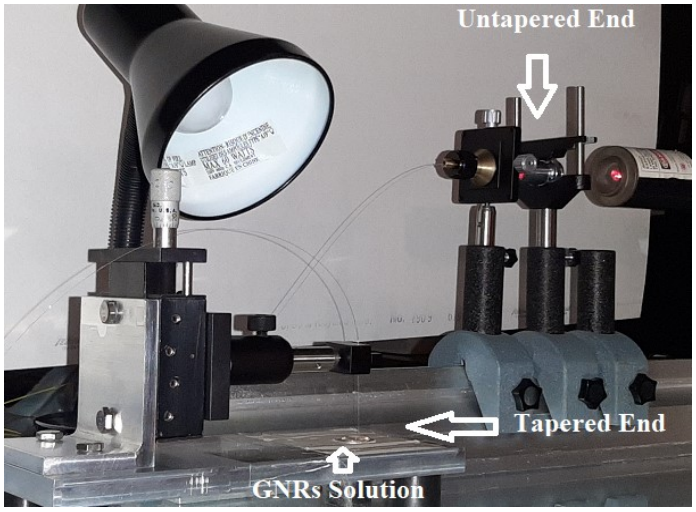

Figure 2.4: Experimental setup for tweezing GNRs using a laser.

The tapered fiber was investigated by a SEM, and the surface of the tapered fiber was found to be rough, with depressions resembling potholes. For tweezing, 250 µl of the colloidal GNR solution was placed on a microscope coverslip. The tapered fiber was then dipped into the solution, and laser light was coupled at the untapered end of the fiber. During the tweezing process, GNRs filled the potholes, and the rods were held in place by Van der Waals force [52]. Once the laser was turned off, the tapered fiber was removed from the fiber holder. When the tapered fiber was put back into the solution for a second time for tweezing, it was expected that some of the GNRs would go back to the solution, or the distribution of the GNRs would be

disturbed. But the effect was not noticeable as the coupled laser also produced a gradient and scattering forces. To further verify those results, the authors dipped a tapered fiber, after tweezing, into the GNRs solution with no laser applied and left it for an hour. The SEM image does not show any significant change in the distribution of the GNRs. Thus, the insertion of the tapered fiber in the GNRs solution for double tweezing did not disturb the periodic structure of the GNRs on the tapered fiber.

2.3 Single wavelength tweezing (1064 nm)

A number of experiments were performed to see the distribution of GNRs on the fiber surface using single wavelength tweezing (either 632 nm or 1064 nm). Figure 2.5 shows the tapered fiber covered with GNR rings when tweezed with a 1064 nm laser of 8.5 mW. It is very clear from the image that GNRs are distributed in the form of rings along the tapered fiber within a certain range with varying periodicity. Different GNR distributions were observed depending on the laser wavelength used.

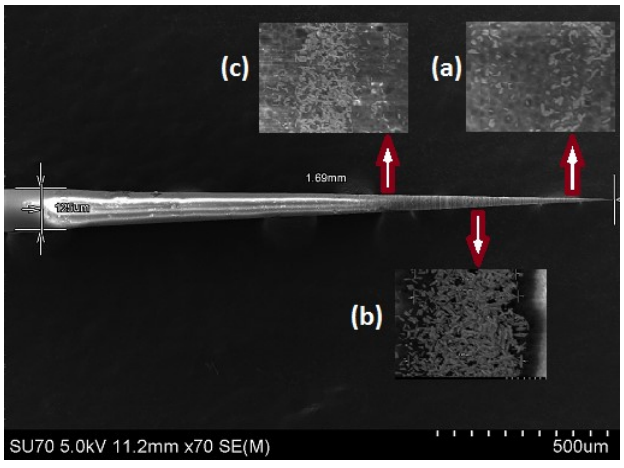

Figure 2.5: SEM image representing the distribution and density of GNR rings in three different segments (a) near the tip (~100 nm – 16 µm), (b) middle region (16 µm – 30 µm), and (c) end region (30 µm – 45 µm) of the tapered fiber.

When the laser was coupled at the untapered end of the tapered fiber, the EM wave propagates through the fiber and reaches the tapered end. The evanescent wave interacts with the GNRs and produces both scattering and gradient forces. The magnitude of the forces depends on the strength of the electric fields due to the evanescent waves, which are different at different diameters of the tapered fiber as the number of modes supported at a particular diameter is different. Further, the optimum coupling of light at the untapered end of the fiber is required as it determines the number of modes excited inside the fiber. Figure 2.6 shows the number of modes supported by the fiber vs. the diameter of the fiber at different locations of the tapered fiber. Further, the number of modes supported by a fiber is related to the V number, which is also related to the diameter of the fiber given in equation 7 in Chapter 1.

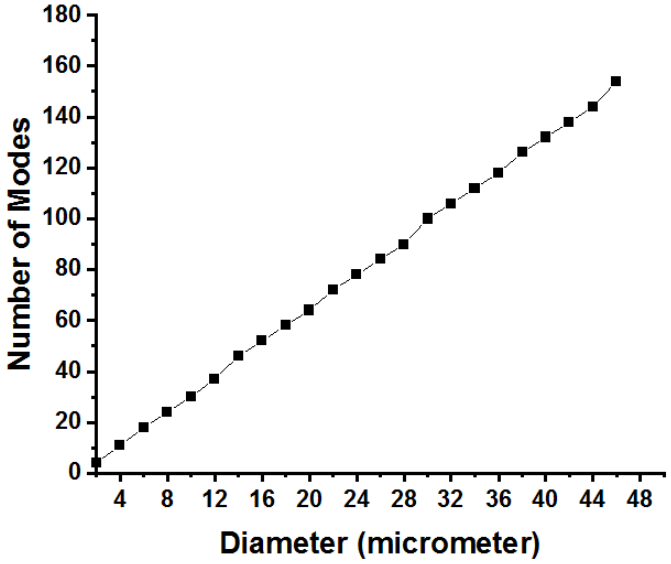

Figure 2.6: Graph showing the number of modes supported by the fiber vs. the diameter of the fiber at different locations of the tapered fiber.

The number of modes at a particular diameter and the interference of their fields in the surrounding medium determines the resultant field and thus decides the magnitude of the

gradient and scattering forces, which determines the distribution of GNRs (light or dense) along the tapered region of an optical fiber as shown in the inset images of Figure 2.5.

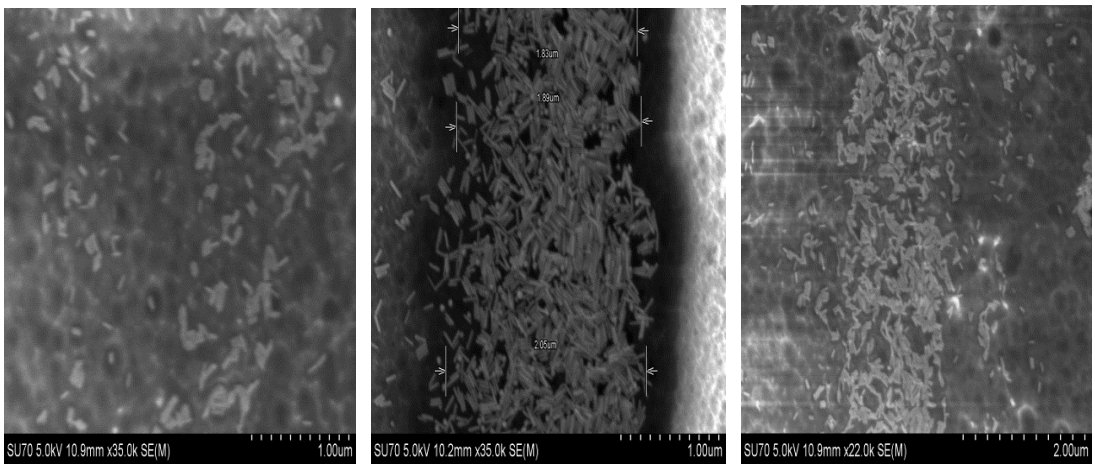

Figure 2.7: SEM images showing the distribution of GNRs near the tip (tip region – 16 µm approx.), in the middle region (17 µm – 34 µm approx.), and at the end (35 µm – 58 µm approx.) of the tapered fiber where GNRs are present along the tapered fiber.

Figure 2.7 shows the variation in the density of GNR rings in three different segments of the tapered fiber. It was noticed that the density of GNR rings at both lower and higher diameters is less compared to the middle region of the tapered fiber. The length of all three segments along which GNR distribution is present depends on the coupling efficiency of the laser light.

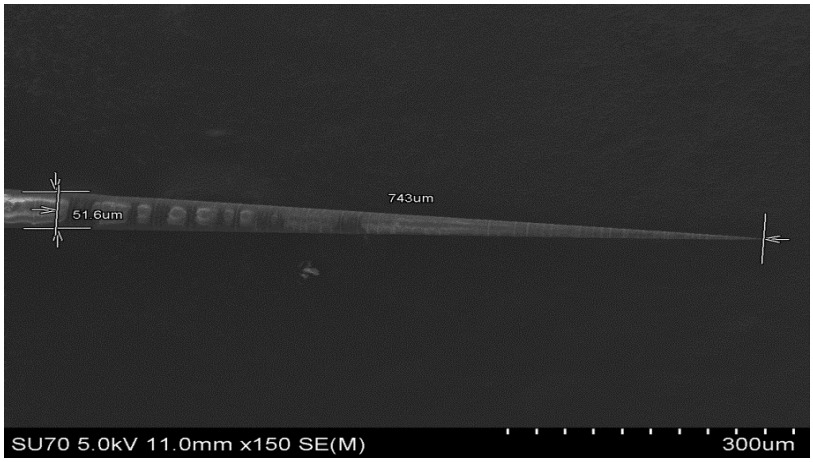

(a)

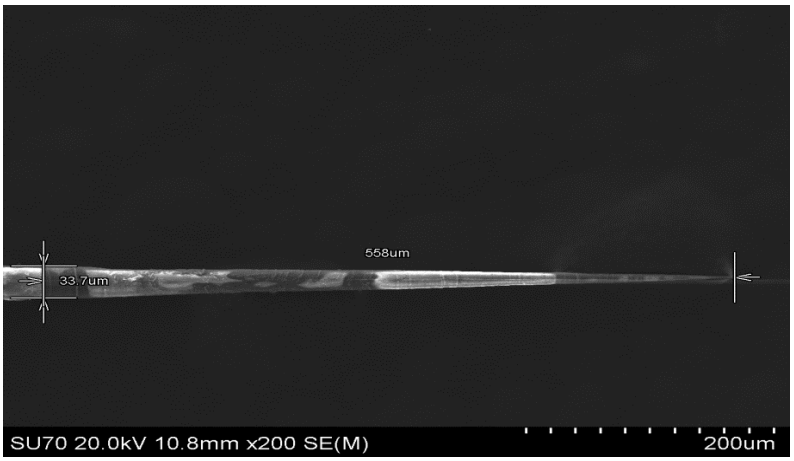

(b)

Figure 2.8: SEM images showing the length of the tapered fiber along which GNR rings are present.

Figure 2.8 (a) and (b) show two tapered fibers covered with GNRs. Although a 1064 nm laser with 8.5 mW power was used, comparing the first and the second sample, the distribution of GNRs are different. In the first sample, the distribution of the GNRs was observed up to a diameter of 51.6 μm, and the length of the tapered fiber covered with GNRs was 743 μm. The

second sample had a GNR distribution up to a diameter of 33.7 μm, and the length of the tapered fiber covered was 558 μm. This difference was due to the coupling efficiency of the laser at the untapered end.

2.3.1 Distribution of GNRs near the tip of the tapered fiber (~ 16 μm)

It is important to discuss how the distribution of GNRs changes near the tip of the tapered fiber, which is on the order of nanometers. From figure 2.9, it can be observed that at lower diameters (∽ 962 nm), the width of the GNR rings were large, and the distribution of GNRs was low in density. However, as the diameter increased, the width of the GNR rings was reduced, and the distribution of GNRs in the rings became more dense. Smaller diameters support very few modes inside the core, and maximum power escapes in the surrounding medium, which results in more scattering power and propels the GNRs away from the fiber surface.

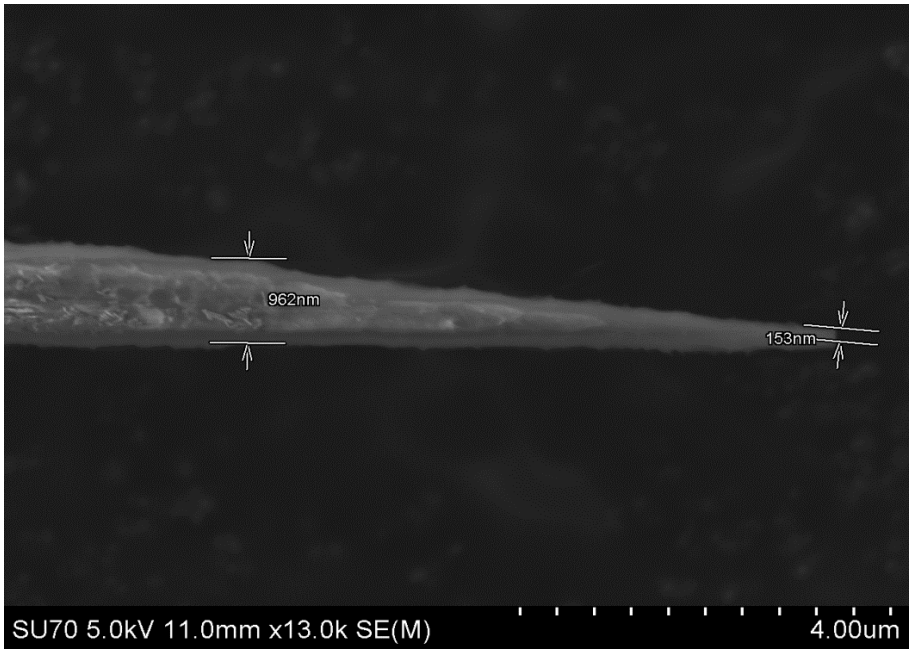

(a)

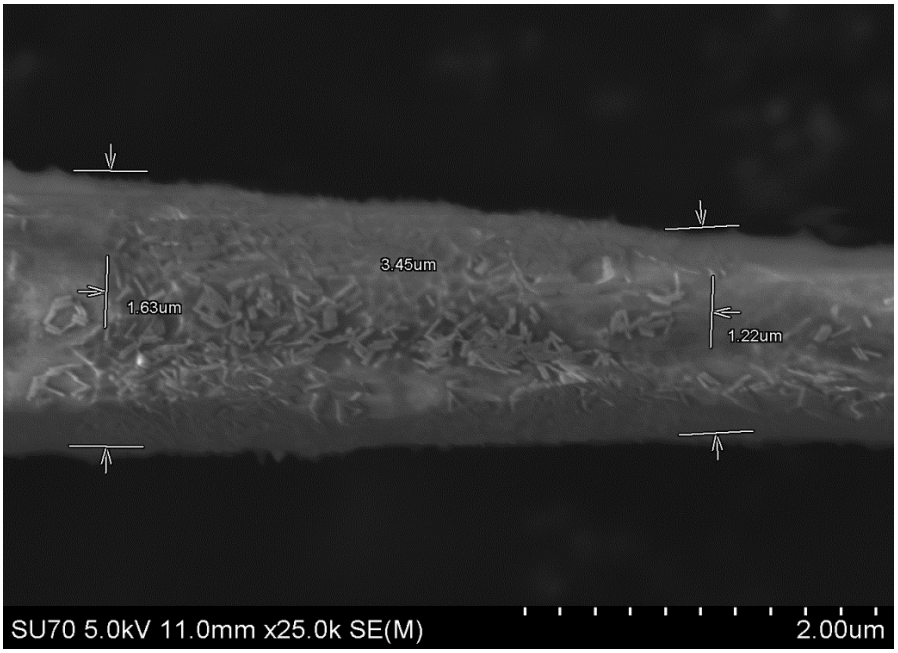
3.45um
1.63um
1.22um
SU70 5.0kV 11.0mm x25.0k SE(M)
2.00um

(b)

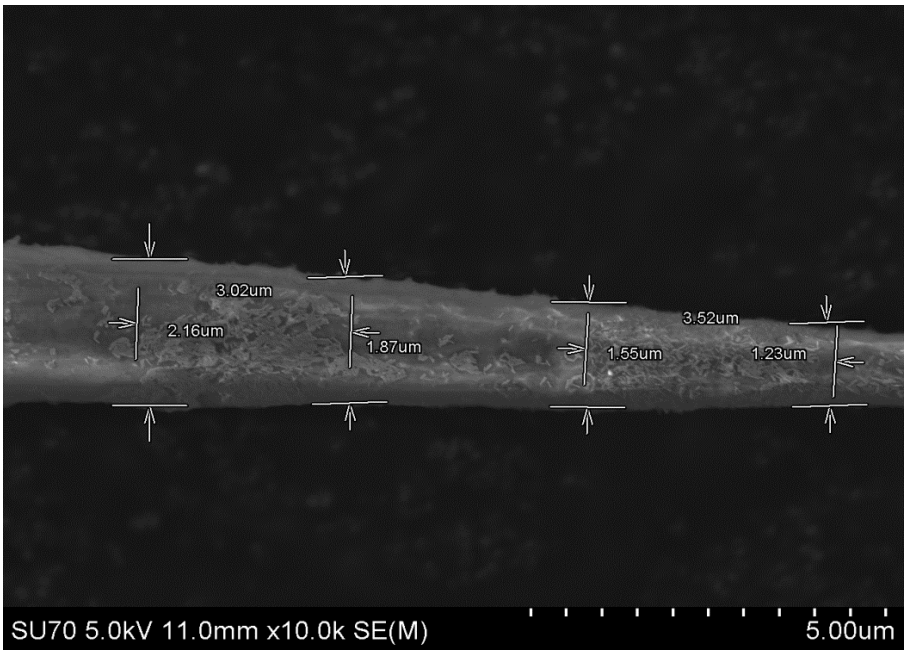
3.02um
2.16um
1.87um
3.52um
1.55um
1.23um
SU70 5.0kV 11.0mm x10.0k SE(M)
5.00um

(c)

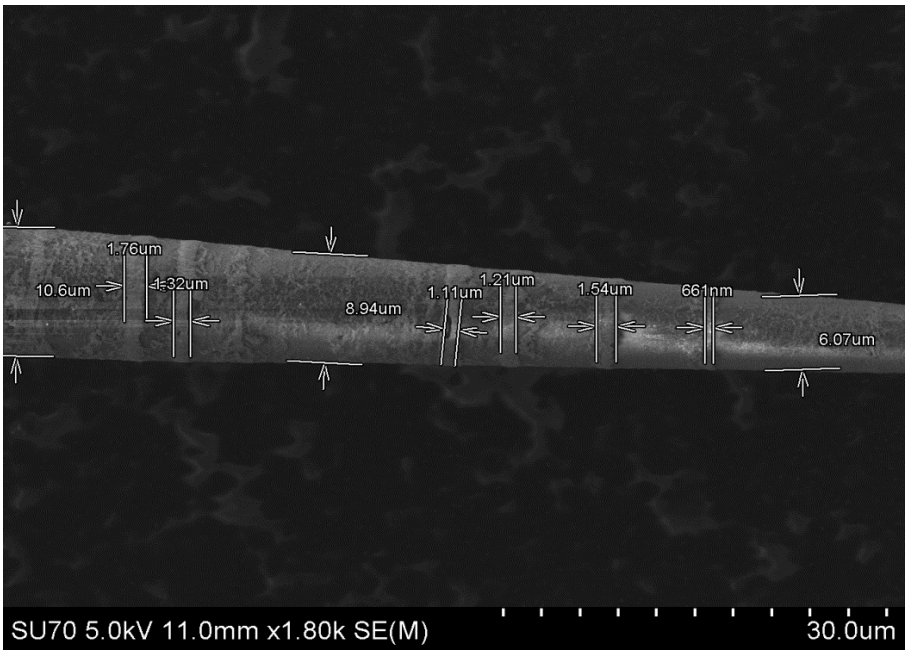

(d)

Figure 2.9: SEM images showing the variation of the width of GNR rings near the tip with respect to the diameter of the tapered fiber.

Figure 2.9 (a) shows that the GNRs first appeared at a diameter of 962 nm, near the tip of the tapered fiber, whereas the tip diameter was 153 nm. Now from Figure 2.9 (b), as the diameter increased to 1.22 μm, the width of the GNRs ring had a width of 3.45 μm where a very light distribution of GNRs was observed. At higher diameters, the width of the rings decreased, such as at a diameter of 2.16 μm, the width of the GNR ring was reduced to 3.02 μm. After a certain point, the width of the GNR rings decreased and became relatively constant ($\backsim$ 1.21 μm in width) and more dense compared to the tip of the fiber as shown in Figure 2.9 (d).

2.3.2 Distribution of GNRs in the middle region of the tapered fiber (17 µm – 34 µm)

It was discussed previously that as the diameter of the tapered fiber increases, the distribution of GNRs becomes more dense, and the width of the GNR rings become nearly identical. After performing several experiments, it is roughly estimated that the consistency in the GNR rings appeared at a diameter of 16 - 20 µm approximately, as shown in Figure 2.10.

In figure 2.10, it is shown that consistent and dense rings are present in the middle region of the tapered fiber. Also, it is seen in figure 2.11 that the separation between GNR rings increased after a particular diameter (∽ 37.6 µm), and the density of those rings was decreased. This above phenomenon occurs because the number of modes varies with the diameter of the tapered fiber.

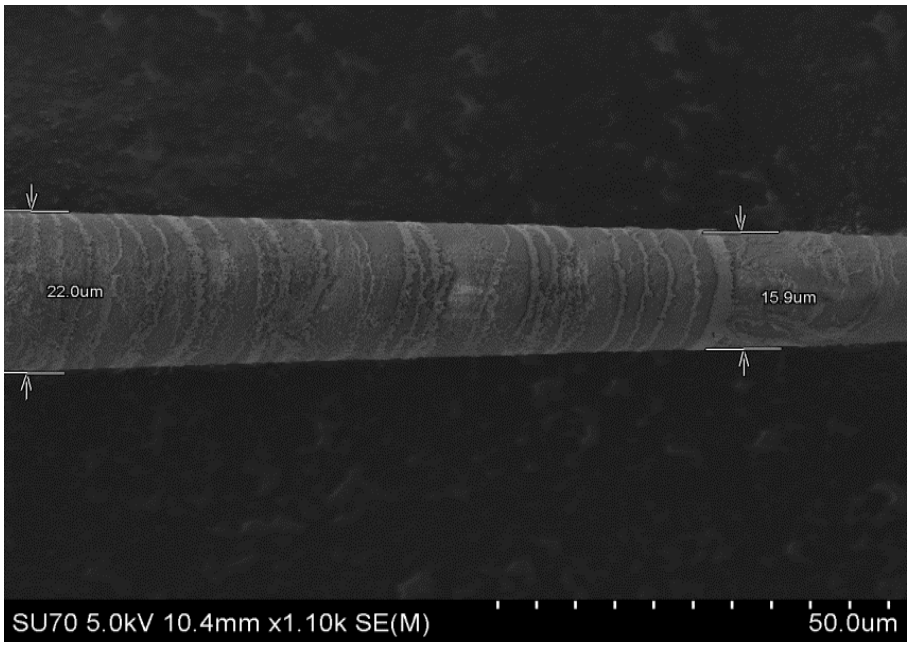

(a)

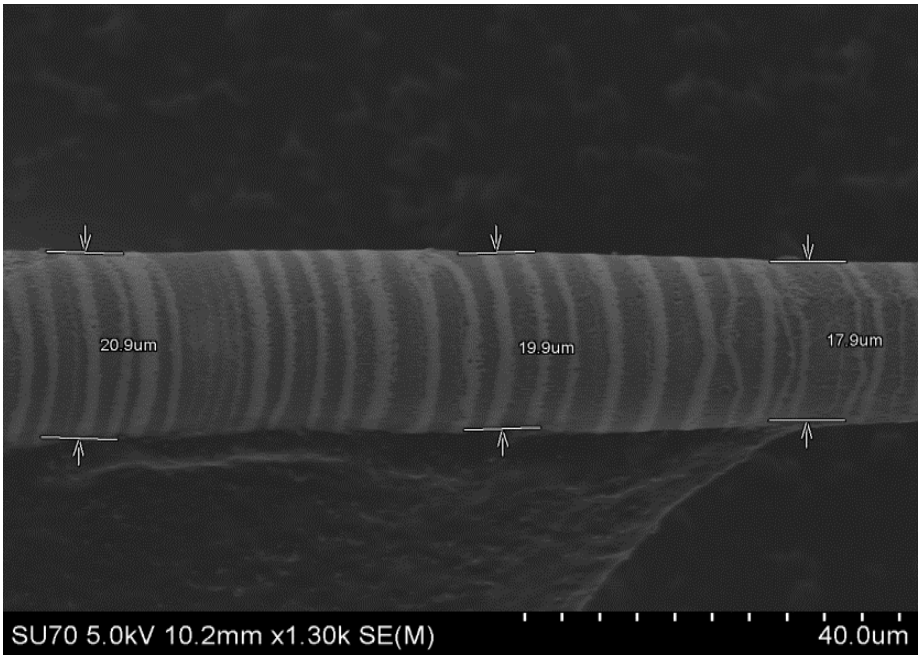

(b)

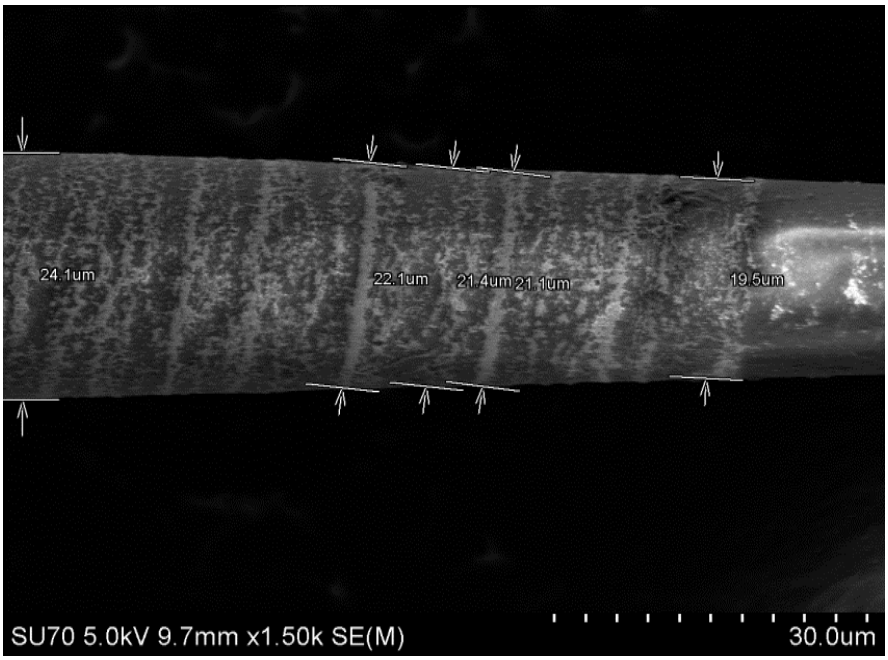

(c)

Figure 2.10: SEM images of 3 different samples showing the middle region of tapered fiber from where the rings appear are more consistent and dense as compared to the rings near the tip.

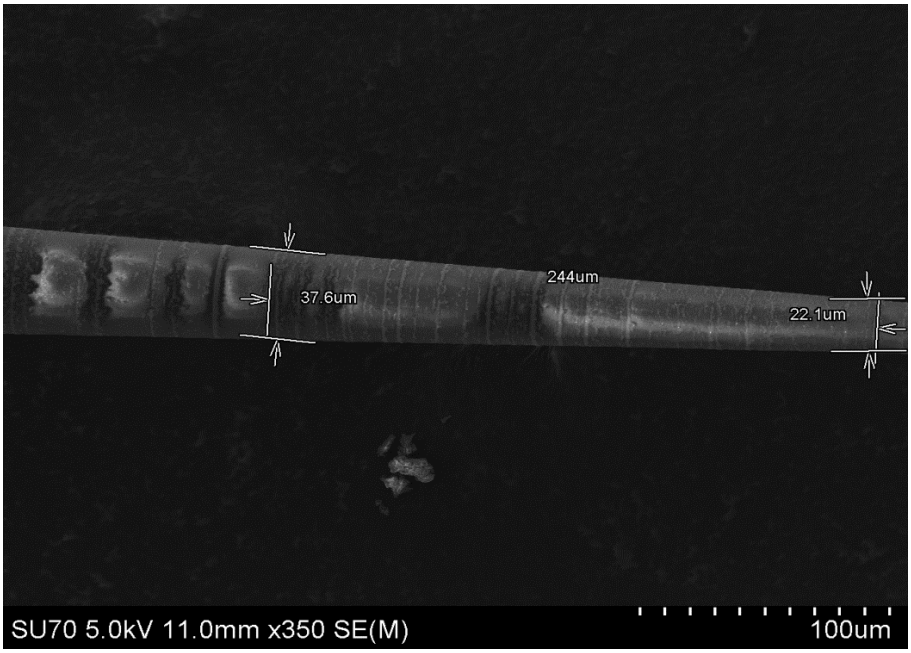

(d)

Figure 2.11: SEM image showing the distribution of GNR rings in the middle region 22.1 – 37.6 µm.

2.3.3 Distribution of GNRs in the end region of the tapered fiber (35 µm – 58 µm)

The GNR distribution in the middle region ends in the diameter range of 35 – 40 µm, as shown in Figure 2.11. Again this not only depends on the laser wavelength or power, but also the coupling of light, which plays an important role in getting the distribution of GNRs as the number of modes excited varies accordingly.

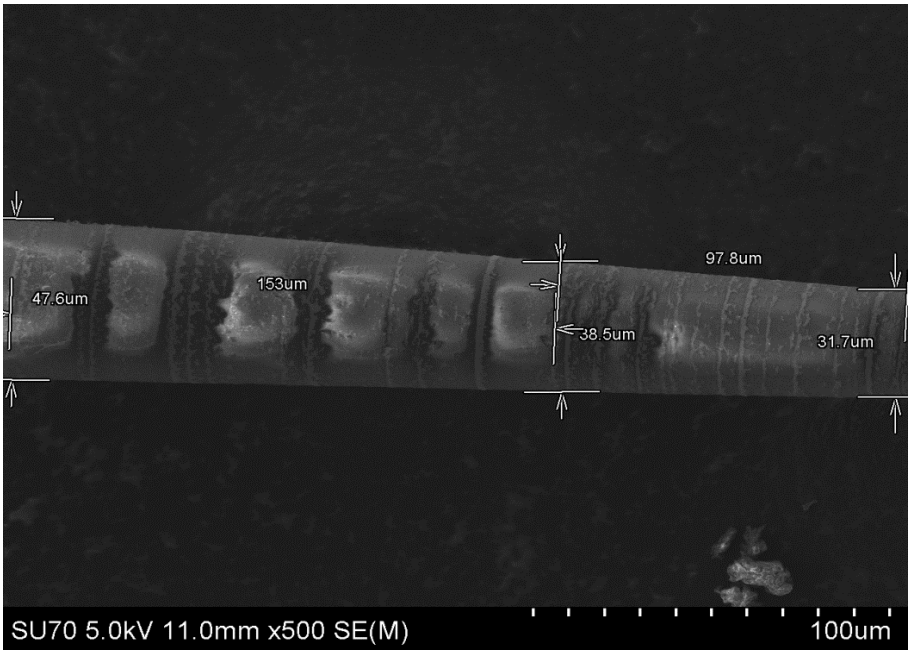

Figure 2.12: SEM image showing how the distribution and separation between two GNR rings changes after a particular diameter (38.5 μm) of the tapered fiber.

As shown in Figure 2.12, fewer GNR rings with a lower density of GNRs and more separation between them were observed in the diameter range of 38.5 μm and 47.6 μm along the tapered length of 153 μm. To justify the presence of fewer GNRs in the end region of the tapered fiber, it is crucial to study the number of modes leaking out in that region of the tapered fiber. It is clear from Figure 2.6 that at large diameters more modes are confined in the fiber core and do not interact with the outer environment, and thus do not produce enough gradient force to overcome the scattering force to trap GNRs on the fiber surface. Figure 2.13 shows that very light GNR rings were present in the end region, along with randomly distributed GNRs.

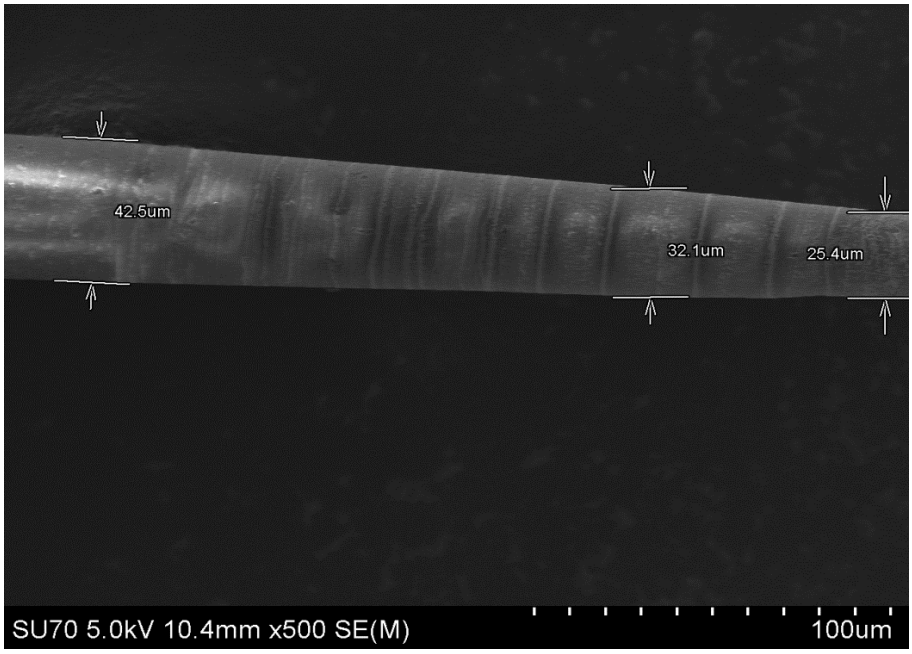

(a)

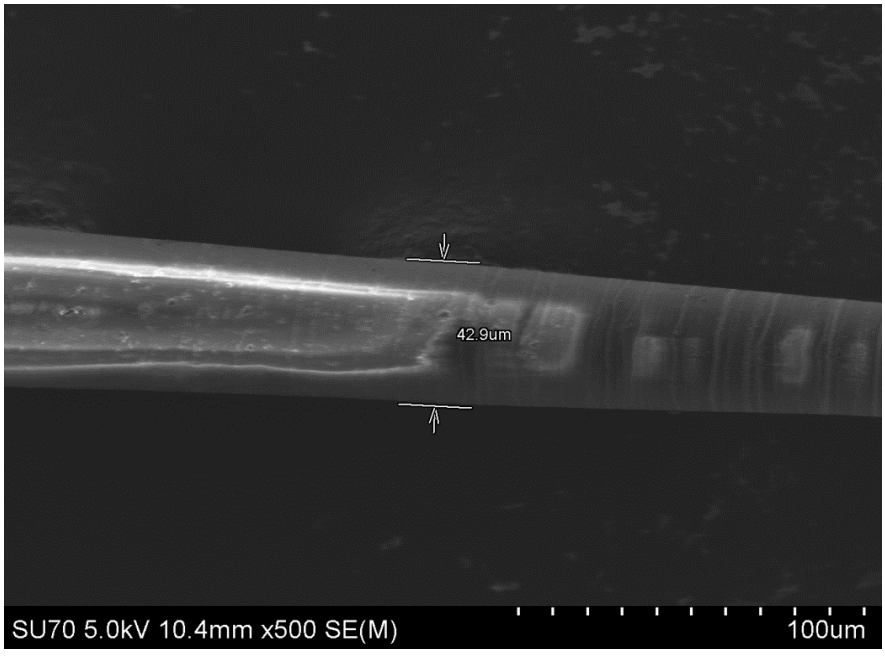

(b)

Figure 2.13: SEM image showing the particular diameter of the tapered fiber where the last distribution of GNRs has been seen.

It is evident from the SEM images that more consistent and dense GNR rings are present in the middle region. Figure 2.14 shows the width and separation between two GNR rings in the middle region. The average separation between two GNR rings in Figure 2.14 (a) and (b) is 2.57 μm, and 2.50 μm, respectively and the average width of GNR rings is 1.45 μm and 1.42 μm, respectively.

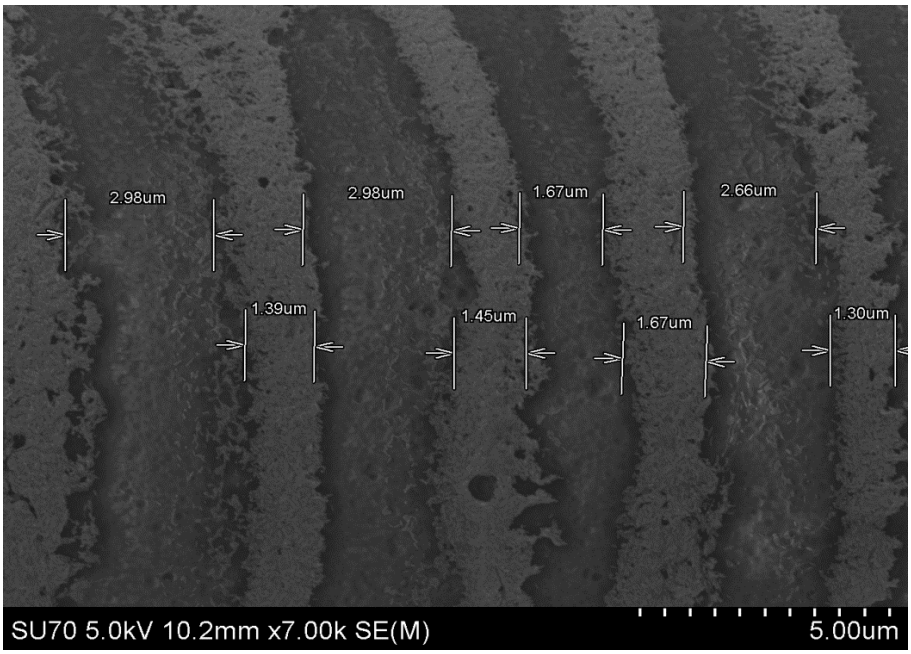

(a)

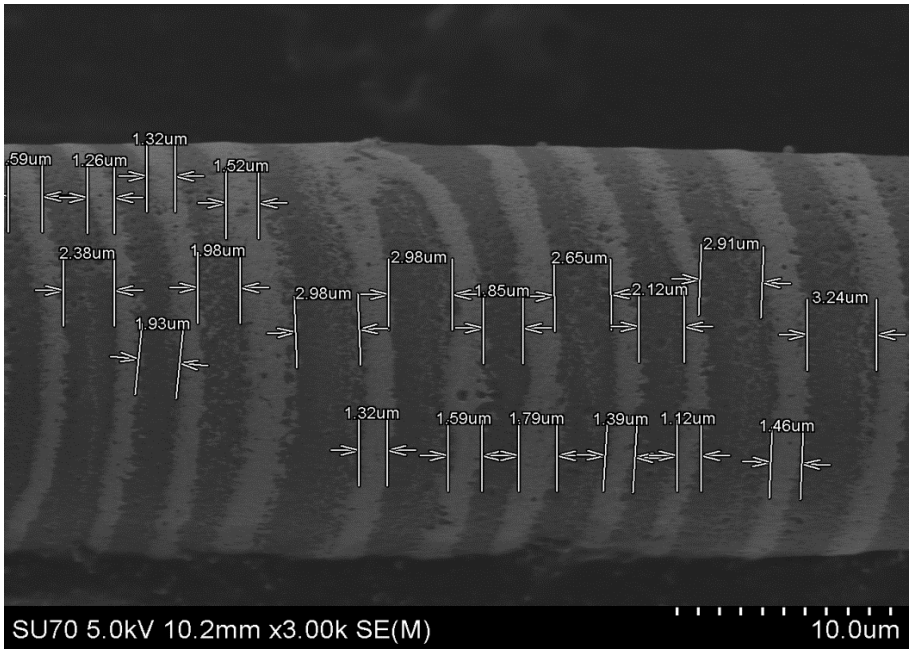

(b)

Figure 2.14: SEM image showing the width of GNR rings and separation between them in the middle region of the tapered fiber.

2.4 Single wavelength tweezing with 632 nm laser

The Experiments were also performed to see the GNRs distribution when a 632 nm laser with 10 mW power was used for tweezing. It was observed that GNR rings were absent, and the random distribution of the GNRs was present along the tapered fiber length (figure 2.15). This experimental result shows that even though the fiber supported more modes at 632 nm compared to when excited with a 1064 nm laser, they were more confined in the core. In other words, the evanescent field was much stronger in the case of a 1064 nm laser compared to a 632 nm laser.

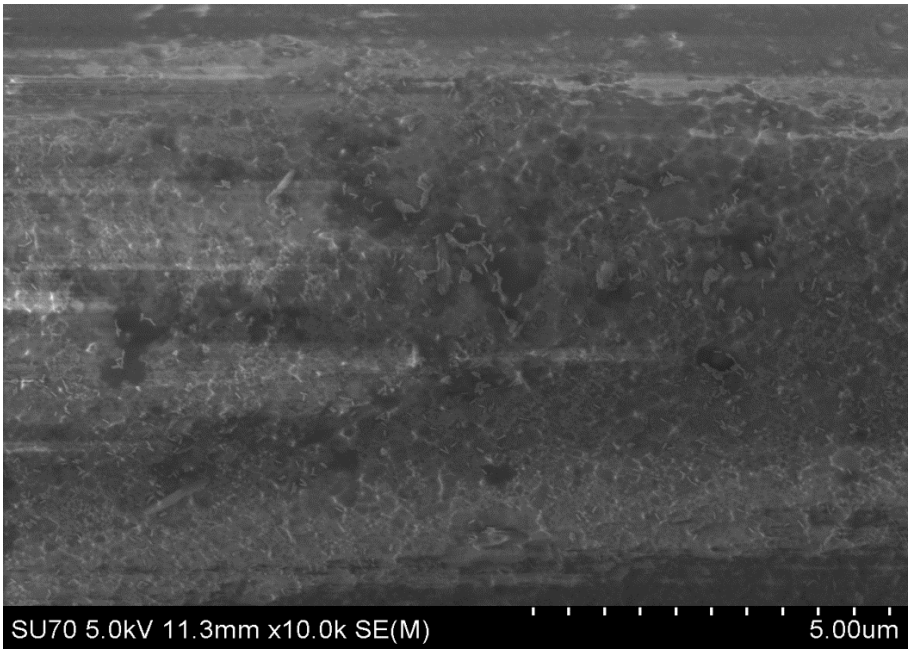

(a)

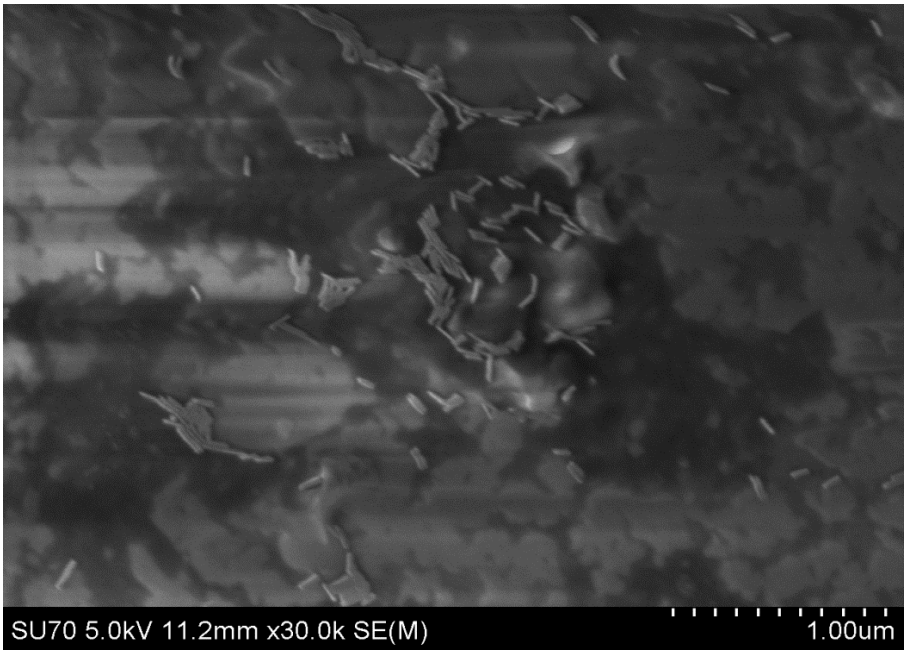

(b)

Figure 2.15: SEM images showing the random distribution of GNRs on the fiber surface when tweezed with 632 nm laser (10mW).

2.5 Double wavelength tweezing (1064 nm and 1064 nm)

It was a challenge to get the distribution of the GNRs close to the tip of the tapered fiber. To manipulate the GNR distribution structure on the fiber surface, and to obtain distribution closer to the tapered end, the tapered fiber was tweezed twice consecutively with a 1064 nm laser as shown in figure 2.16. It was investigated that GNR rings with smaller periodicity are present during double wavelength tweezing as compared to the single wavelength tweezing case. In figure 2.16 (b), there were lighter GNR rings present between the two denser rings.

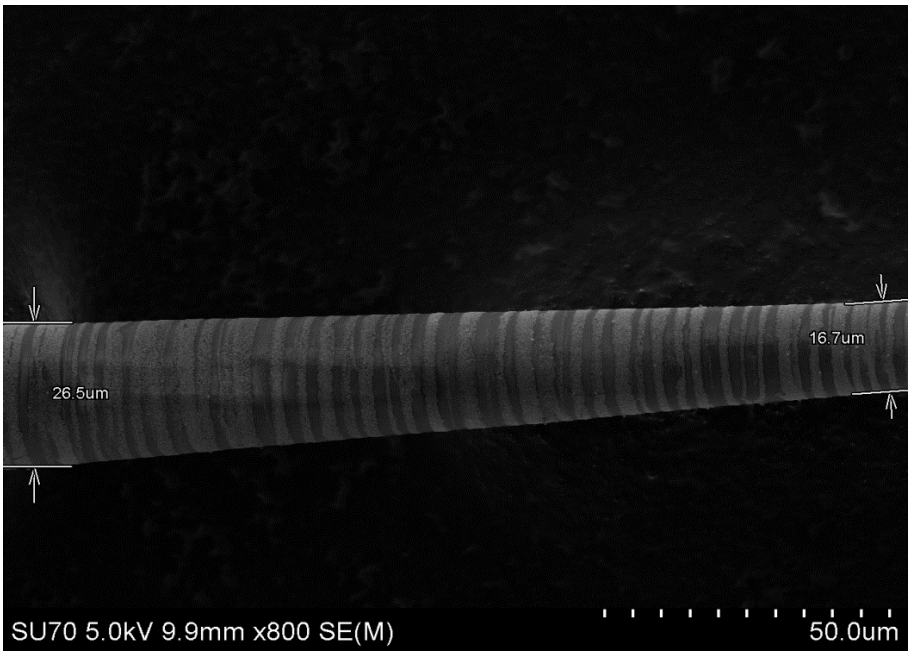

(a)

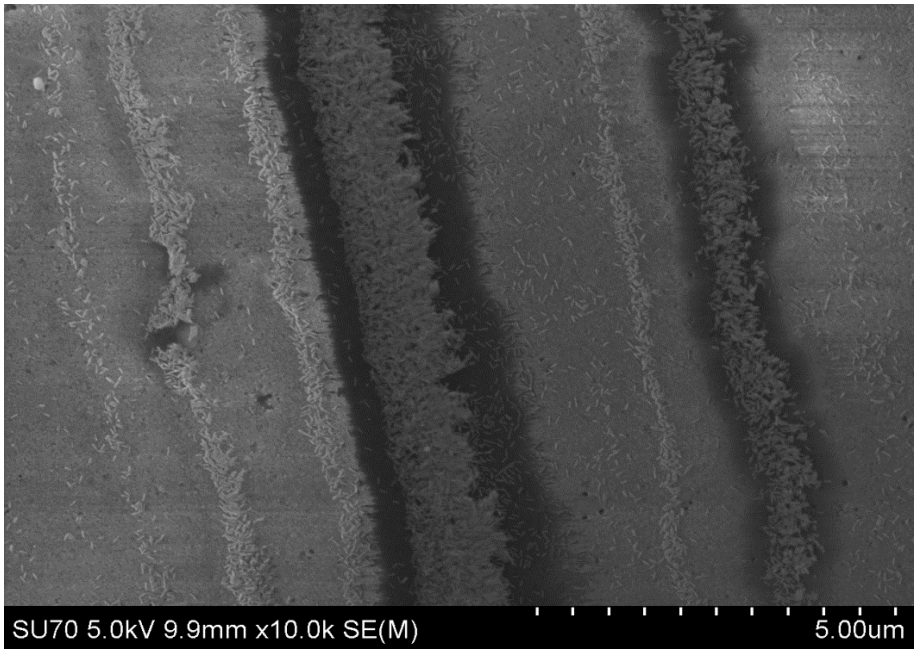

(b)

Figure 2.16: SEM images showing (a) the segment of the middle region (b) presence of lighter rings between denser GNR rings of the tapered fiber when tweezed two times with 1064 nm laser consecutively.

In figure 2.17, although more GNR distribution was observed in double tweezing, the shape of the GNRs was destroyed in some places. Figure 2.17 (b) shows the distortion of the GNRs shape. This is due to the excessive heat produced by the absorption of the 1064 nm laser (Longitudinal LSPR wavelength for the GNRs at 1064 nm) by the GNRs deposited on the tapered fiber after the first tweezing. A lower input laser power during the second tweezing process can eliminate the damage. GNRs should be intact to take advantage of their excitation at the LSPR wavelength for Raman spectroscopy.

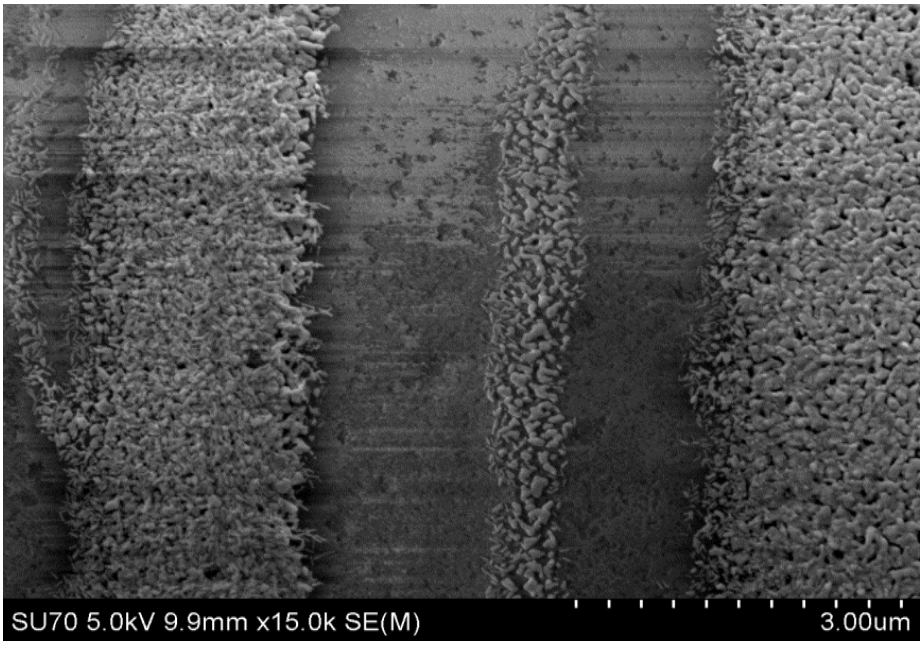

(a)

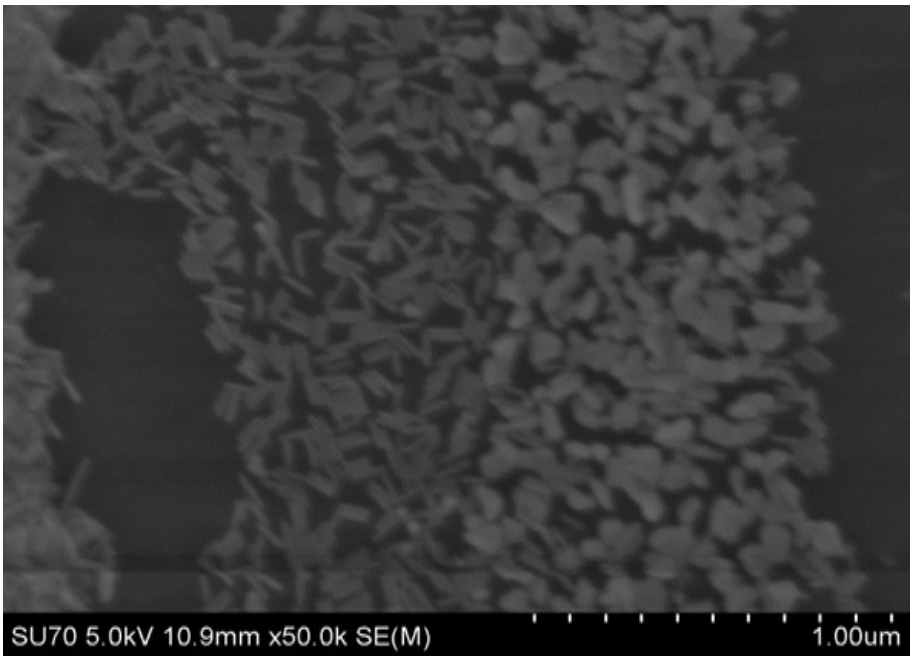

(b)

Figure 2.17: SEM images showing the destroyed shape of GNRs during double tweezing (1064 nm)

2.6 Double wavelength tweezing (1064 nm and 632 nm)

Another experiment was conducted to see the results shown by the tweezing with two different wavelengths, 1064 nm and 632 nm, consecutively. Then results were compared with the distribution of GNRs when either the 1064 nm or 632 nm wavelength laser alone was used for tweezing. The periodic structure was observed to begin at a smaller diameter (∽ 4μm) (figure 2.18), whereas in the case of single tweezing with a 1064 nm laser, consistent and dense rings were observed to begin at a larger diameter (∽ 16μm) (figure 2.10). When tweezed with a 1064 nm laser, GNRs covered the tapered fiber, which then acted as a waveguide for the 632 nm light to propagate without leaking and thus allowed more power to propagate through the fiber and closer to the tip. Therefore, the modes at smaller diameters have enough power to produce a gradient force and pull the GNRs onto the fiber surface.

Furthermore, the interference pattern at smaller diameters was different from that at larger diameters, as the number of modes supported by the smaller-diameter fiber was lower compared to the larger diameter. Thus, we obtained different periodicity in the distribution. Also, it is noticeable that in the case of double tweezing, a random distribution of GNRs lies between the denser GNR rings on the tapered fiber surface (figure 2.19). In this case of double, tweezing with two different wavelengths (632 nm and 1064 nm), the maximum surface area of the fiber is covered with GNRs, and GNRs shape are intact as well. As a larger portion of the tapered fiber is covered with GNRs, it can act as an excellent substrate for Surface-Enhanced Raman scattering. The separation between GNR rings and the width of those rings was investigated by SEM (figure 2.19). The average width and separation was 1.02 μm and 2.59 μm, respectively. Along with the GNRs dense rings, there was a lighter distribution of GNRs between those rings, which makes

the tapered fiber surface an efficient substrate for Surface-Enhanced Raman Spectroscopy (SERS).

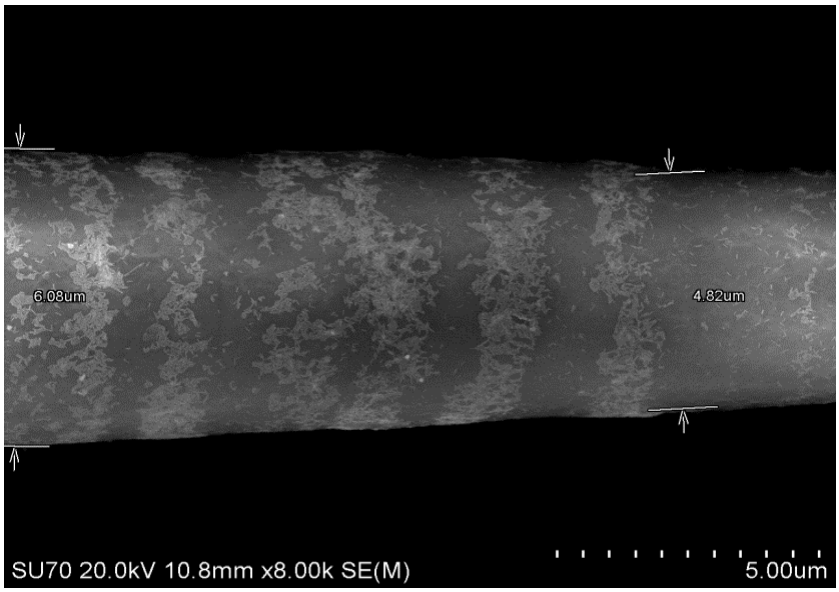

(a)

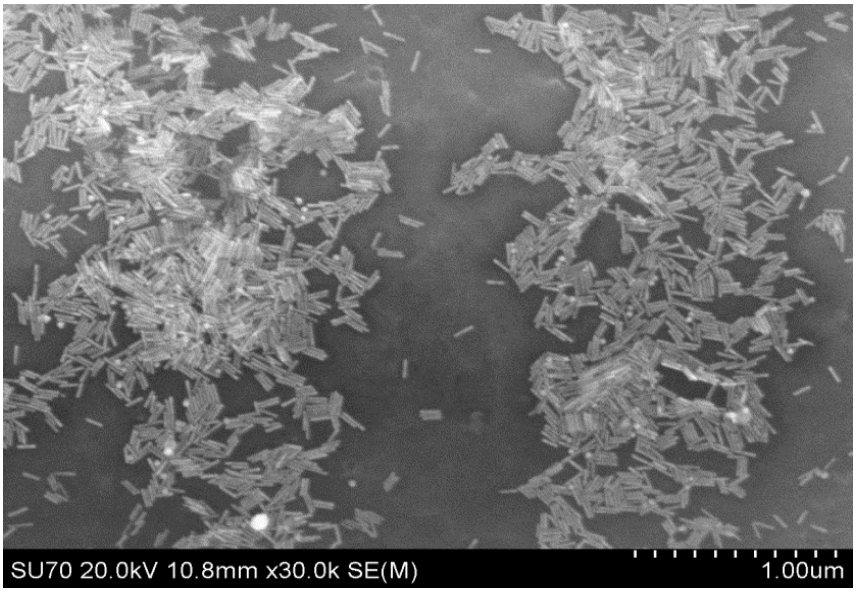

(b)

Figure 2.18: SEM images showing (a) the ring structure of GNRs even at the smaller diameter and (b) the distribution of GNRs at the same location.

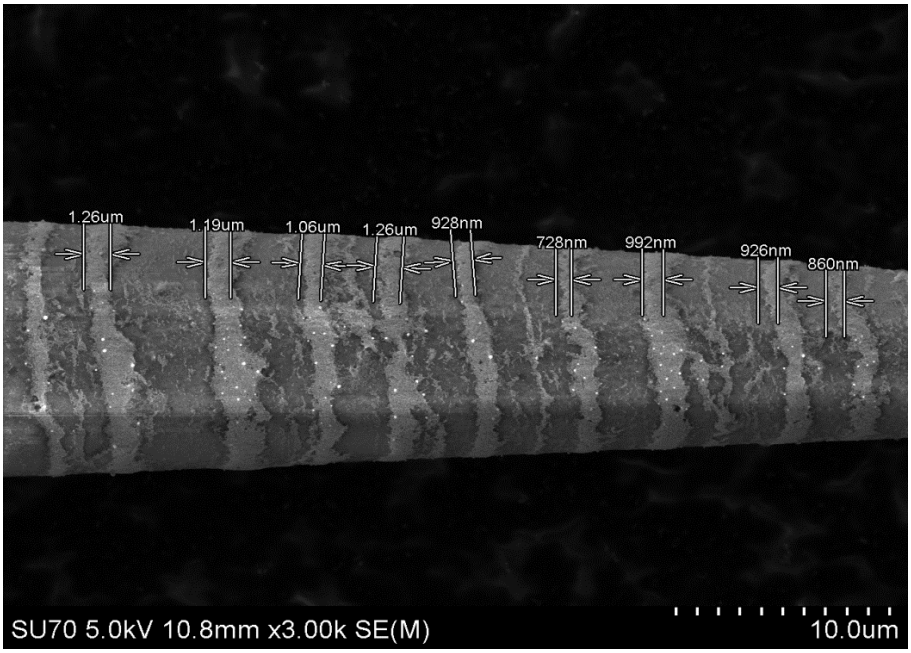

(a)

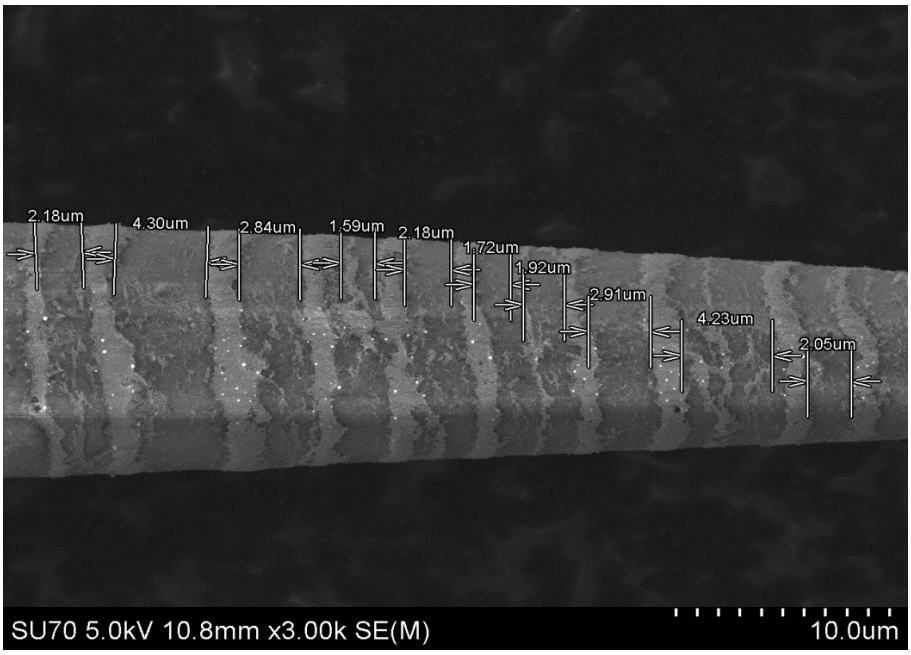

(b)

Figure 2.19: SEM image showing the (a) width of the GNR rings and, (b) separation between two rings when the fiber is tweezed with 1064 nm and 632 nm consecutively.

2.7 Effect of cone angle and length on the distribution of GNRs on the fiber surface

To investigate the effect of the tapered fiber length and cone angle on the distribution of GNRs when tweezing with a single wavelength (1064 nm), two samples were prepared with lengths 1.49 mm and 0.804 mm. In both cases, a periodic distribution of GNRs was obtained. As can be seen in Figure 2.20, a segment of approximately 54 μm has been studied for each fiber length. This segment began at a diameter of 13 μm (approximately) in each case to compare the number of modes in that specific portion of the probe. Furthermore, in Figure 2.20 (a) (length = 1.49 mm), the number of modes supported by the fiber at the beginning (13 μm diameter) and end (8.60 μm diameter) of the 54 μm region are 42 and 28, respectively. The number of modes leaking out of the fiber along this section was thus 42-28 = 14. In Figure 2.19 (b), (length = 0.804 mm), the number of modes supported by the fiber at the beginning (13 μm diameter) and end (3.42 μm diameter) of the 54 μm region are 42 and 10, respectively. The number of modes leaking out of the fiber along this section was thus 42-10 = 32. So, when the length of the tapered fiber is short, and the cone angle is large, the number of modes leaking out of the fiber is quite large (i.e. 32), which means high power is present in the surrounding medium (GNR solution), which can destroy the shape of the GNRs. From experimental data, it has been observed that GNRs were not destroyed when the length of tapered fiber was greater than 1.0 mm. Also, by controlling the coupling of laser light at the untapered end, we can keep the GNR's shape intact. In addition, it is experimentally observed that by decreasing the tapered length, GNR rings can be found at diameters of less than 1 μm, similar to the result seen when tweezing a longer tapered fiber multiple times. Both of these different techniques fulfill the goal of covering the maximum

area of tapered fiber with GNR rings, which minimizes the probability of signal leakage near the tip and increases the surface area of the substrate for SERS application.

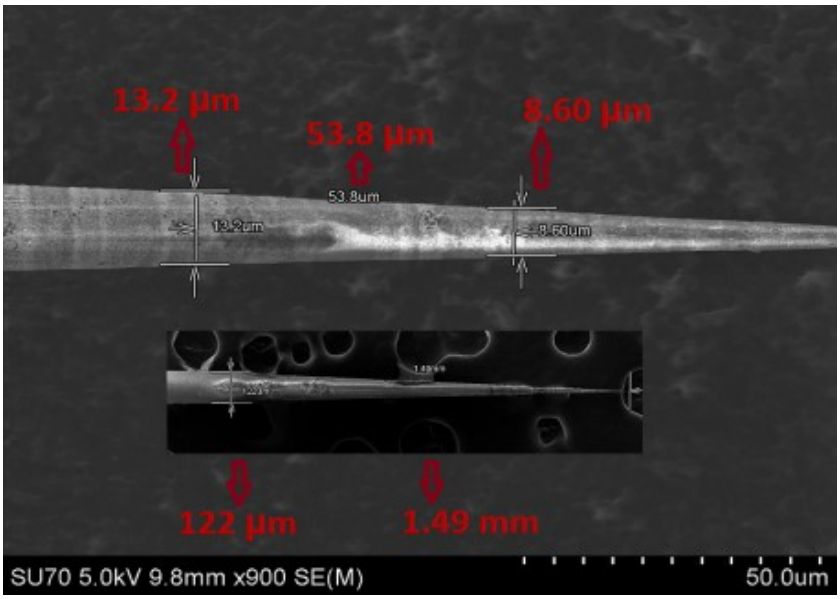

(a)

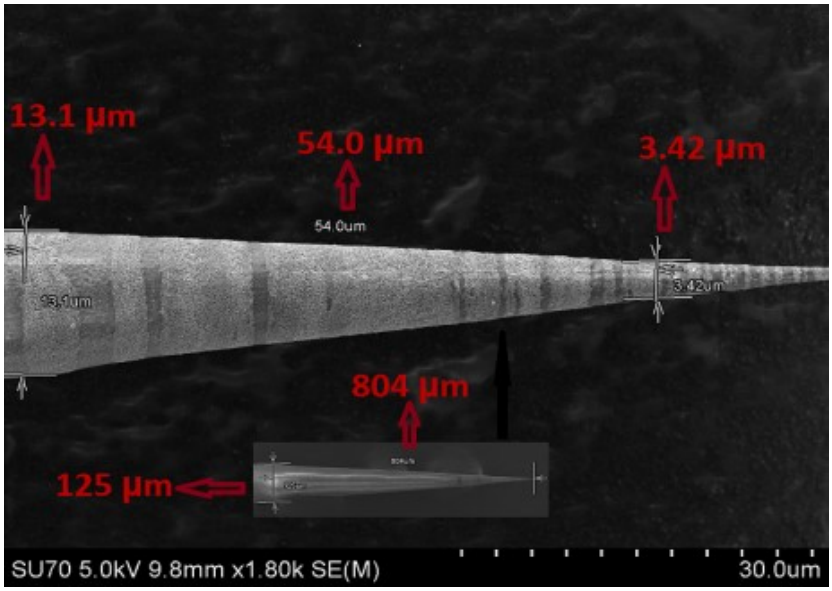

(b)

Figure 2.20: SEM images of two different samples with GNR distribution tweezed by a 1064 nm laser of 8.5 mW power for (a) Taper length = 1.49 mm (b) Taper length = 0.804 mm.

The characteristics of the tapered fiber with different tweezing conditions were investigated using SEM images. We also investigated the tapered fiber's plasmonic structure optically. To study the distribution of the GNRs on the tapered fiber a He-Ne laser (632 nm) was coupled to the untapered end of the fiber. The tapered end was placed under microscope objective. Figure 2.21 (a) was taken using a camera placed at the eyepiece of the microscope, and the distribution of GNRs is visible. The same fiber sample was tested with SEM, and the image confirms the distribution of GNRs (figure 2.21 (b)).

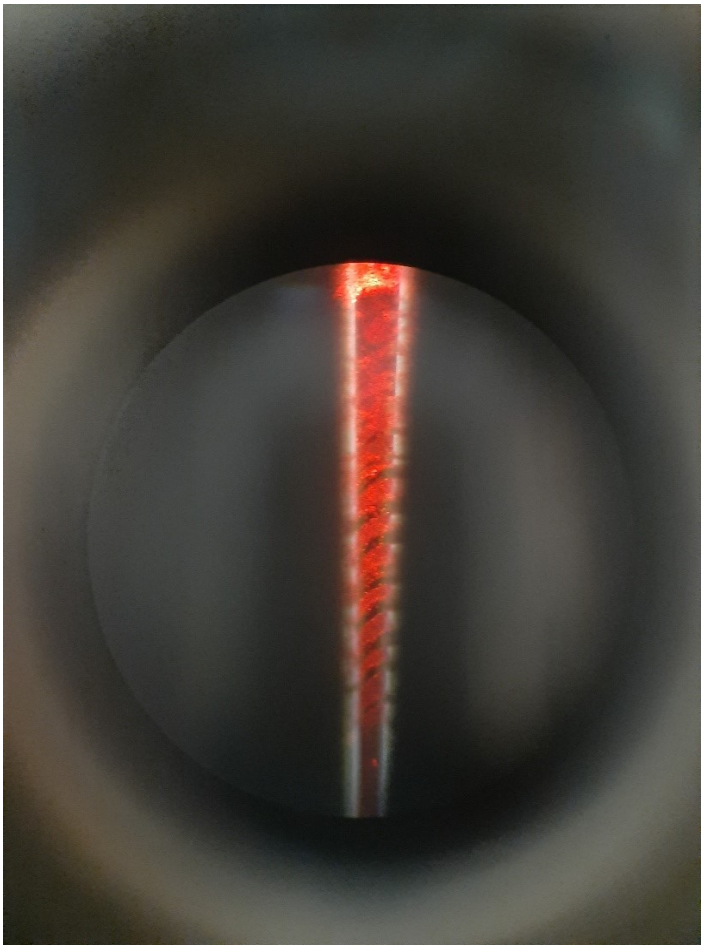

(a)

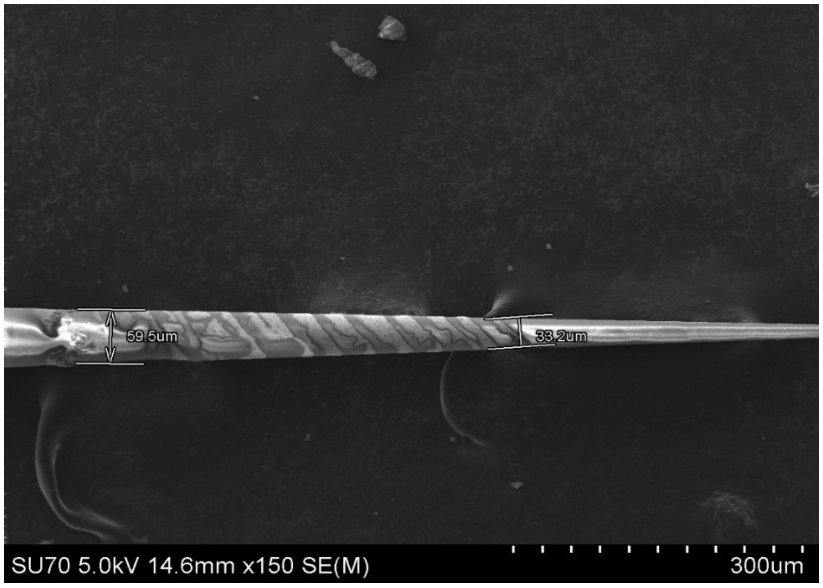

(b)

Figure 2.21: Image was taken using (a) microscope and (b) SEM of the same fiber sample when tweezed with a single wavelength (1064 nm) laser.

2.8 Conclusion

The method of preparing tapered fiber using HF acid was discussed in detail. An experiment was performed to observe how the tapered length of the fiber changes with the speed of the translational stage. The graph produced a linear trend. The experimental setup for tweezing GNRs on the fiber surface was discussed. In the double tweezing case, the tapered fiber was tweezed with two different wavelengths (1064 nm and 632 nm). Tweezing was performed successfully with both wavelengths. When fiber was tweezed with 1064 nm, a grating like structure was observed. While tweezing with 632 nm, a random distribution of GNRs along the tapered fiber length was noticed. Next, to get the GNRs distribution near the tip of the tapered fiber, the experiment was performed using double tweezing (either with the same wavelength or

different wavelengths). The results obtained from double tweezing using the same wavelength (1064 nm and 1064 nm) indicated that the maximum area of fiber was covered with GNRs, but the shape of the GNRs was not intact.

On the other hand, when double tweezing was performed with different wavelengths (1064 nm and 632 nm), more GNRs were observed on the fiber, and the shape of the GNRs was intact. Also, the width and separation between the GNRs rings were studied in both single and double tweezing. Lastly, the experiment was performed to see the effect of the cone angle and tapered length on the GNR distribution. It was concluded that when the length of the tapered fiber was shorter than 1mm, the GNRs shape was destroyed. Also, it was observed that when the tapered length is shorter, and the cone angle is larger, the maximum area was covered with GNRs near the tip. It minimized the signal leakage near the tip and increased the efficiency of the SERS substrate. Also, the characteristics of the tapered fiber plasmonic structure were observed optically using a He-Ne laser, which shows that we do not need an expensive SEM to see the GNR distribution. The plasmonic structure developed on the tapered optical fiber can be used in applications such as to detecting chemicals at low concentrations.

Chapter 3

Applications of the plasmonic structure as a Surface-Enhanced Raman Spectroscopy (SERS) substrate

3.1 Introduction

It has already been discussed that the intensity of the Raman signal can be enhanced by a factor of 10^{10} when using a Surface-Enhanced Raman Spectroscopy (SERS) substrate [45]. The very first application of SERS was proposed in 1974 when the Raman signal was significantly enhanced using a Silver (Ag) substrate [30;32]. The high adsorbtivity of Silver (Ag) makes the system suitable for SERS. SERS has been used in various applications, for example, detection of explosives at the nanomolar and femtomolar level, and in medical diagnosis [46;48]. In this investigation, gold nanorods (GNRs) with aspect ratio = 6.4 were used to prepare a plasmonic structure on a tapered optical fiber which can be used as a SERS substrate. The high sensitivity and selectivity of the SERS technique allows for the detection of analytes at low concentration adsorbed on a rough metallic substrate. The enhancement of the Raman scattered signal for

chemical and material Rhodamine 6G (R6G) and Graphite, respectively, was explored based on the developed plasmonic structure.

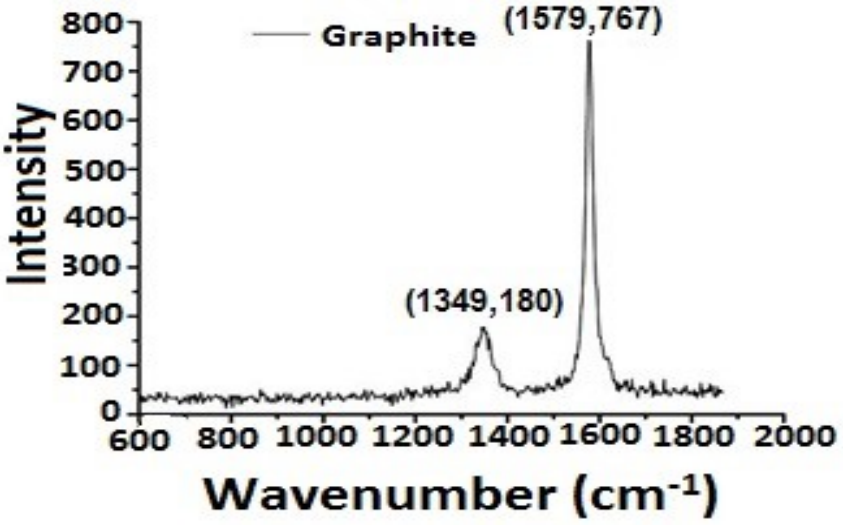

(a)

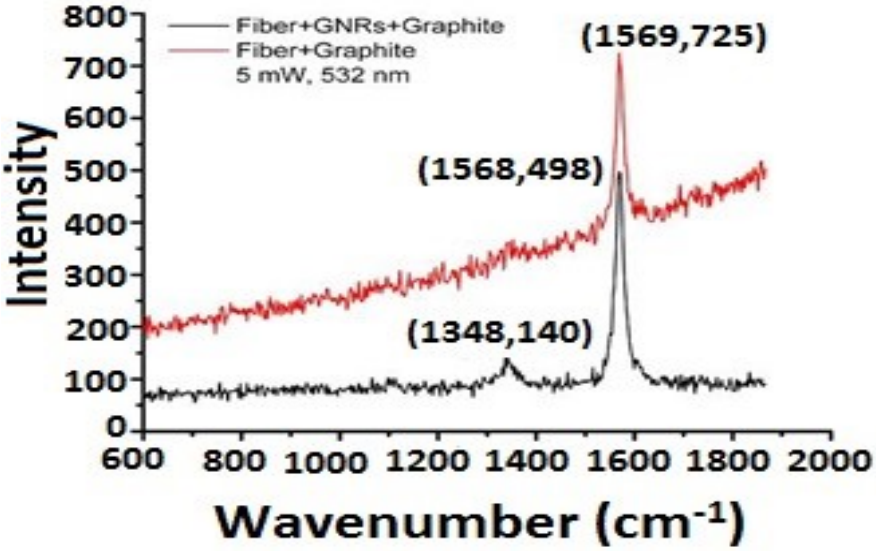

(b)

Figure 3.1: Comparing the Raman Spectrum (collected with a Renishaw Raman Spectrometer) produced by a 532 nm laser using (a) graphite powder (without nanoprobe), and (b) with (black: 1 s exposure) and without GNRs on the surface of the probe (Red: 5 s exposure).

3.2 Raman Spectra of Graphite

To investigate the application of the plasmonic structure as a SERS substrate, we followed two steps. In step one, a few milligrams of Graphite powder was placed on the sample holder without a probe. The Raman Spectra was obtained from the sample (figure 3.1 (a)), which matches with previously obtained results [53].

In step two, the graphite powder was sprinkled on the surface of the tapered fibers, both with and without GNRs. The graphite powder is adsorbed on the surface. Figure 3.1 (b) shows the spectra of Graphite powder in the presence and absence of GNRs. Two peaks were visible when a fiber probe with a GNR distribution was used to obtain the Raman spectrum (Black Spectrum in figure 3.1 (b)), whereas only one peak was visible when there was no GNRs present (Red Spectrum in figure 3.1 (b)). In both cases, the amount of Graphite powder on the fiber probe was extremely small.

Further, in Figure 3.1 (b), the black spectrum was obtained with 1 s exposure, whereas the red spectrum was obtained with 5 s exposure. Thus, the presence of GNRs increased the intensity of the Raman scattered light. In the above cases, to collect the Raman Spectrum, a 532 nm laser was used as the excitation wavelength.

3.3 Raman Spectra of Rhodamine 6G (R6G)

R6G is a highly fluorescent dye. A mixture of 0.2550 mg of R6G and 230 μl of GNR solution was prepared before tweezing with a 1064 nm laser. We took this approach to investigate the applicability of the tweezing process for the analyte, which does not react with GNRs. We were successful in tweezing R6G and GNRs. Figure 3.2 shows the SEM image of the

distribution along the length of the tapered fiber when tweezed with the R6G and GNR solution together with a 1064 nm laser. The length of tapered fiber with GNRs and R6G present was 884 μm. Figure 3.3 shows an enlarged view of a GNRs and R6G band, as well as the presence of GNRs on the flake-like structure of R6G. The average width of the GNR and R6G band was 5.68 μm (figure 3.4 (a)), which was twice the width when tweezing was done with only GNRs. The average separation between the two bands was 11.77 μm, as indicated in figure 3.4 (b). One can reduce the concentration of R6G in the GNR solution to obtain the Lowest Detection (LOD) limit. We believe that tweezing the analyte, which does not react with the GNR solutions, on the surface of the tapered fiber for Raman spectroscopy is an excellent accomplishment of this research.

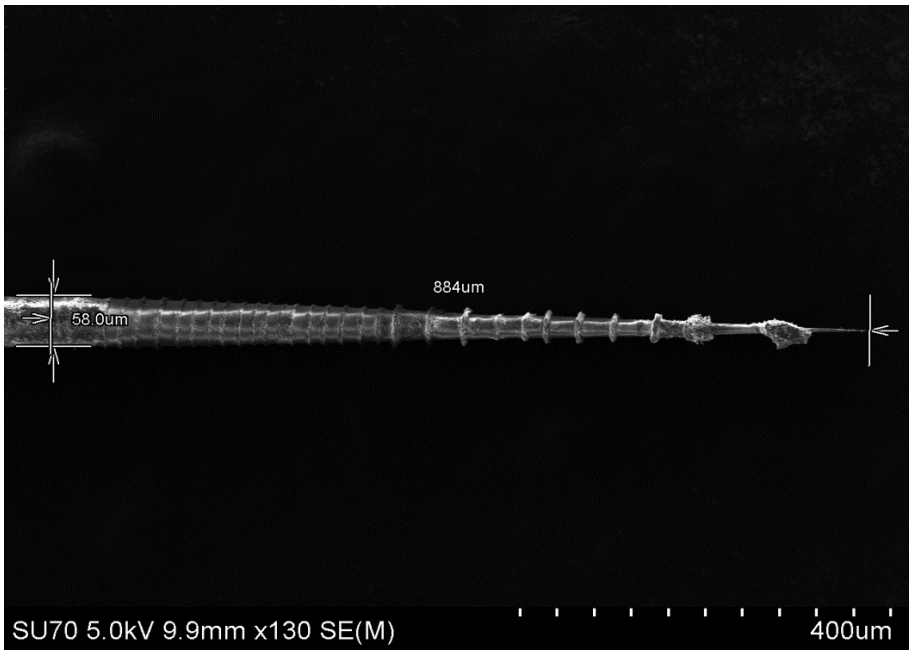

Figure 3.2: SEM image showing the distribution of R6G and GNRs when tweezed together with 1064 nm laser.

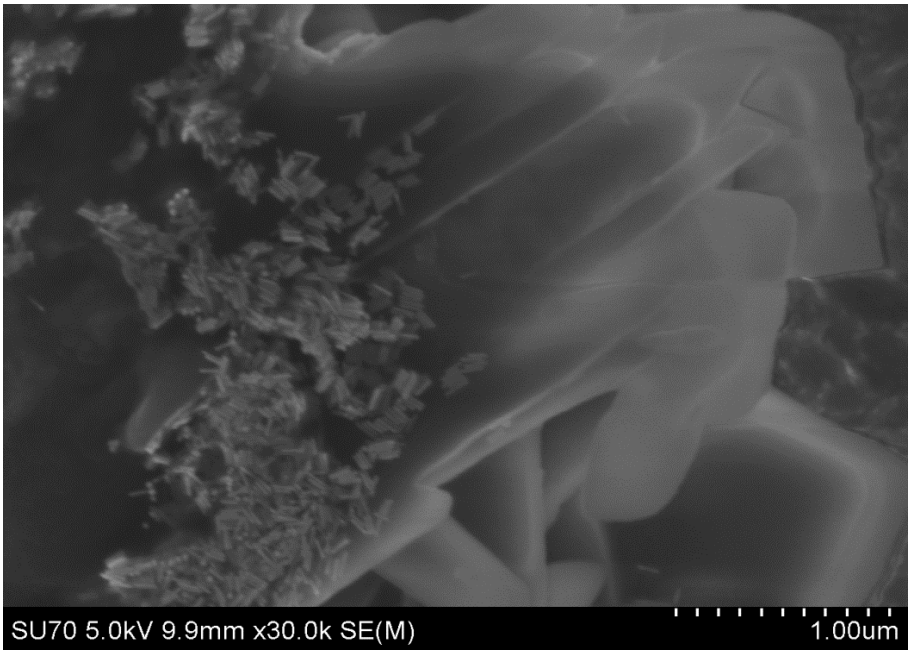

Figure 3.3 SEM image showing the enlarged view of GNRs on the top of R6G flakes.

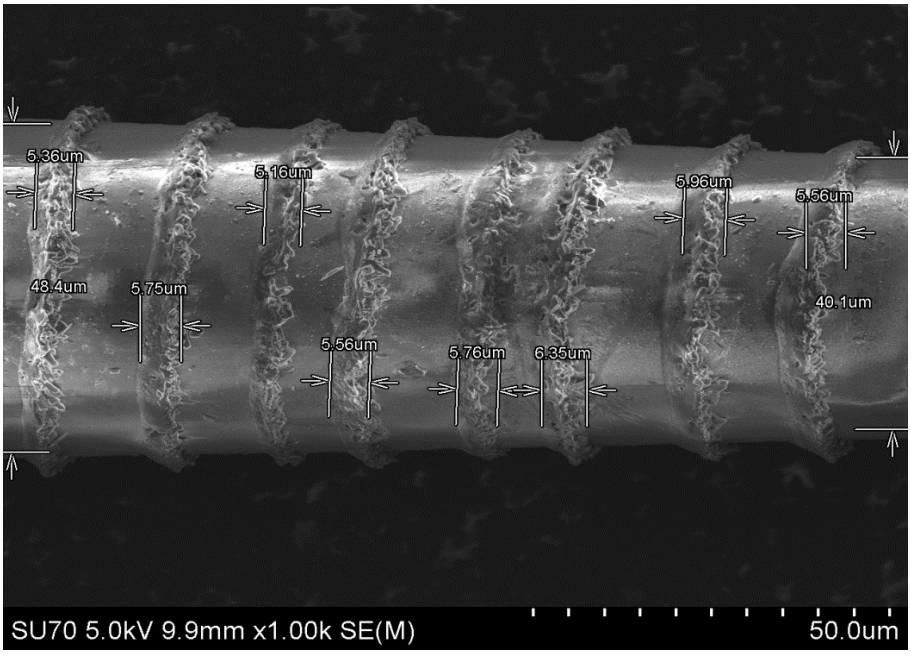

(a)

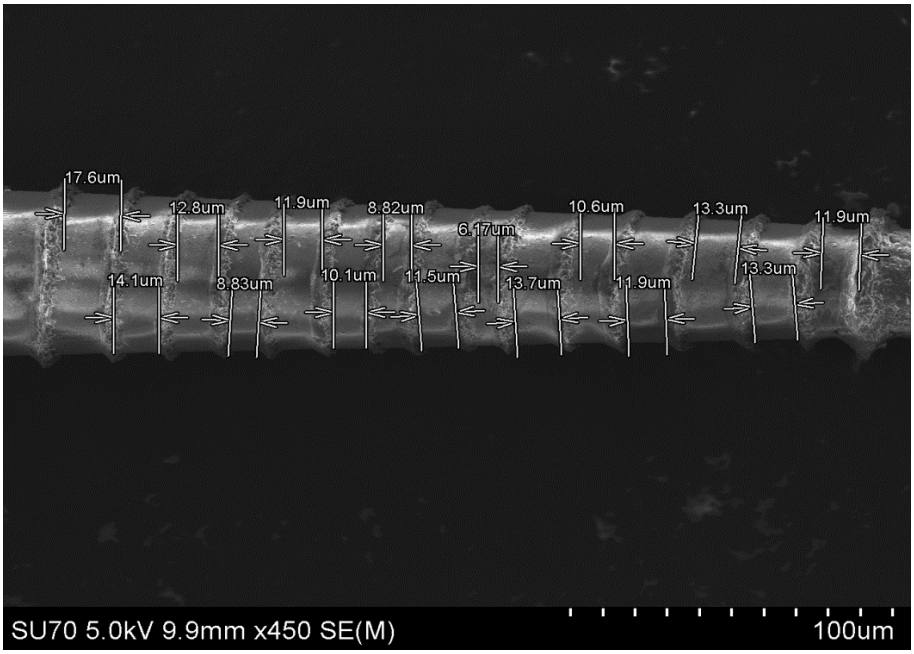

(b)

Figure 3.4: SEM images indicating (a) the width of GNRs and R6G band, and (b) the separation between the two bands.

Figure 3.5 shows the Raman Spectra of R6G. Figure 3.5 (a) was obtained from a few milligrams of Rhodamine 6G (R6G). Figure 3.5 (b) and (c) compare Raman spectra of R6G with and without GNRs present on the tapered fiber probe, respectively. Figure 3.5 (b), was obtained with R6G sprinkled on the bare tapered fiber. Figure 3.5 (c) was obtained with the plasmonic structure prepared by tweezing R6G and GNRs together, as described in the above paragraph on the tapered fiber. A significant enhancement was observed when GNRs were present as the number of peaks observed when compared to the bare fiber with R6G is more numerous and distinct. The observed peaks matched with previously obtained Raman spectra for R6G [54]. The excitation wavelength was 532 nm.

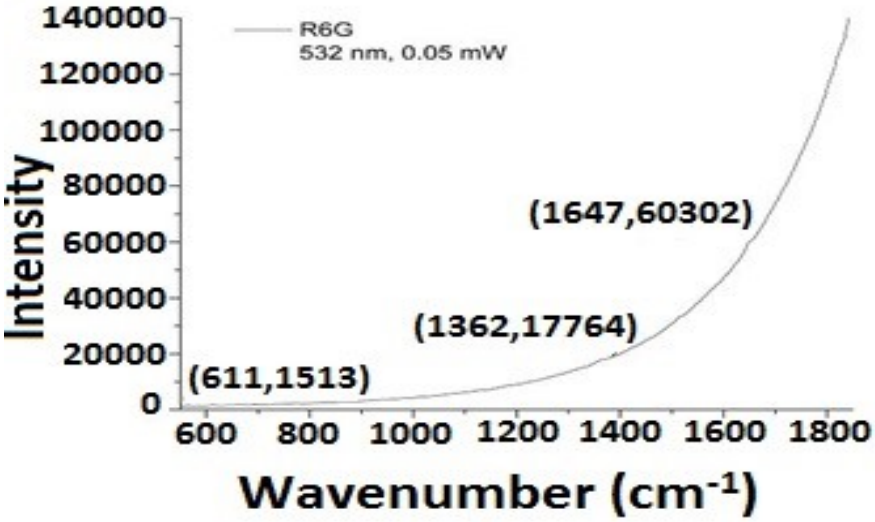
R6G
532 nm, 0.05 mW
Intensity
140000
120000
100000
80000
60000
40000
20000
0
(1647,60302)
(1362,17764)
(611,1513)
600
800
1000
1200
1400
1600
1800
Wavenumber (cm-1)

(a)

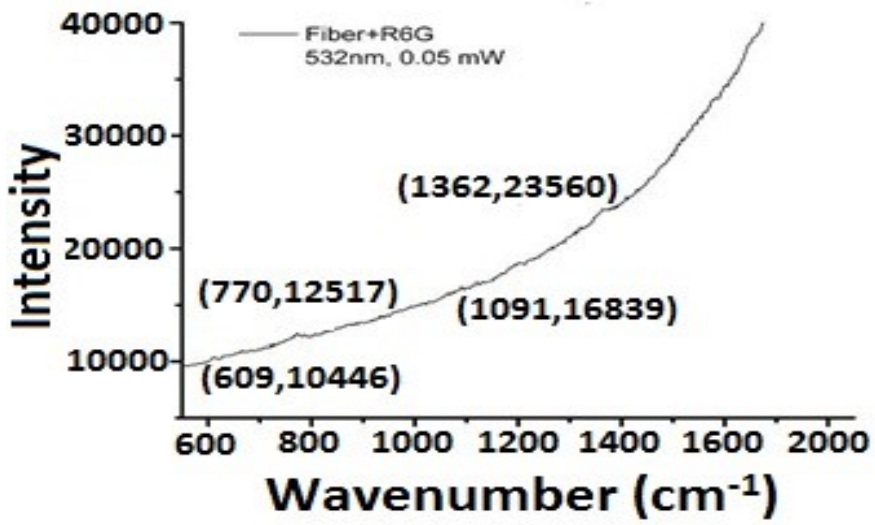
Fiber+R6G
532nm, 0.05 mW
Intensity
40000
30000
20000
10000
(1362,23560)
(770,12517)
(1091,16839)
(609,10446)
600
800
1000
1200
1400
1600
2000
Wavenumber (cm-1)

(b)

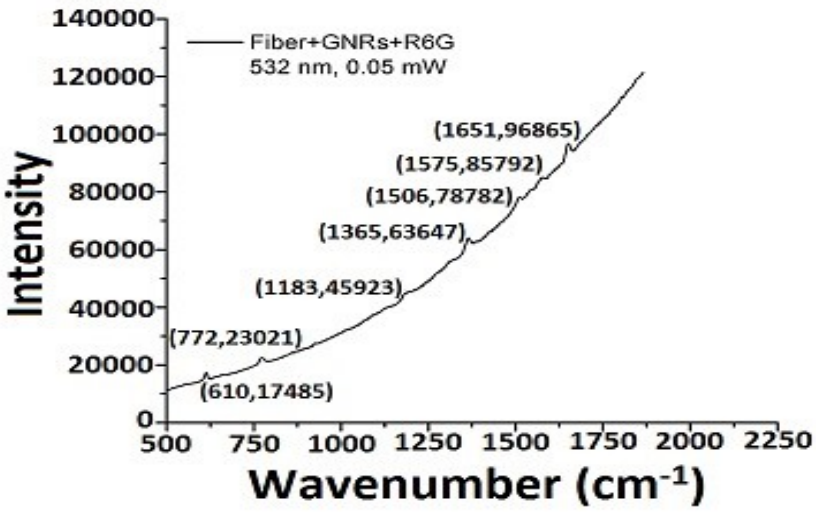

(c)

Figure 3.5: Raman Spectra (collected with a Renishaw Raman Spectrometer) produced by a 532 nm laser using (a) R6G (without nanoprobe), (b) R6G + Fiber and (c) R6G + Fiber + GNRs (1s exposure).

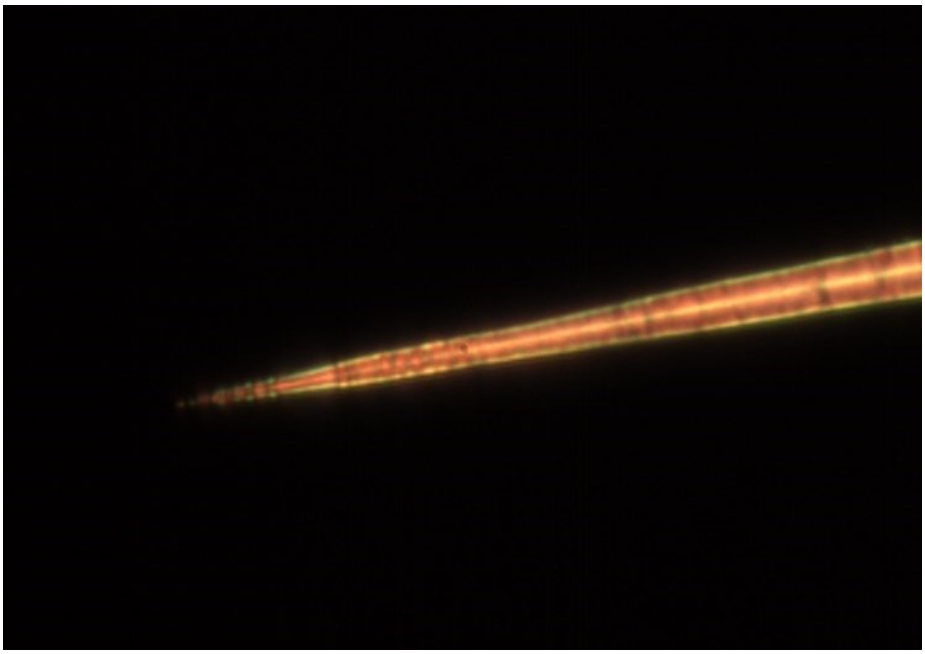

(a)

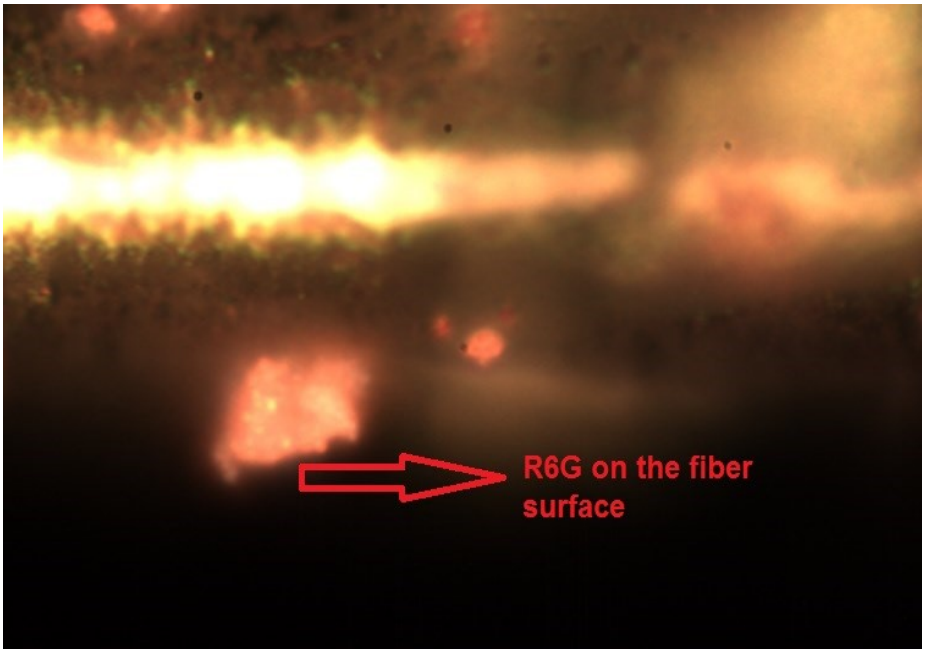

(b)

Figure 3.6: Image from Renishaw Spectrometer microscope (a) when the tapered fiber was focused for excitation by 532 nm laser, (b) the enlarged image of fiber surface where a few chunks of R6G are present.

Figure 3.6 shows an optical image of a tapered fiber with R6G present on it seen by the Renishaw spectrometer. Figure 3.6 (b) shows a magnified view of the fiber where R6G and GNRs are present, and by focusing the light at this location, the Raman spectra for a specific area was obtained. The experimental results show that the presence of GNRs enhanced the Raman signal for both Graphite and R6G. Thus, it can be concluded that the developed plasmonic structure can be used as a SERS substrate.

3.4 Conclusion

In conclusion, it was observed that a tapered fiber plasmonic structure with GNRs of aspect ratio = 6.4 could be used as a SERS substrate to enhance a weak Raman signal. Figure 3.1 and 3.5 shows the Raman spectra for Graphite and R6G (chemicals adsorbed on the fiber surface using single wavelength tweezing (1064 nm)) and, distinguishable peaks are visible with the GNRs present on the fiber surface. The Raman spectra can be obtained by coupling the excitation laser from the untapered end of the tapered fiber SERS substrate, and collecting the Raman scattered light using a microscope objective.

Chapter 4

Application of tweezing metal compound and future work

4.1 Introduction

In Chapter 2, optical tweezing of GNRs on the tapered fiber surface was discussed in detail and also, the characteristics of the plasmonic structure along the fiber length were studied through SEM as well as using an optical microscope. It was also shown in Chapter 3 that a combination of an analyte (R6G in this case) and the colloidal GNR solution can be tweezed onto the tapered fiber surface. In this chapter, we present the results obtained by tweezing a compound on the fiber surface. The experiment was performed by mixing Zinc Hydroxide ($Zn(OH)_2$) with the colloidal GNR solution.

4.2 Tweezing of Zinc Hydroxide ($Zn(OH)_2$)

We investigated the possibility of tweezing analytes which contain different metal ions and produce a plasmonic structure on the tapered fiber for Raman Spectroscopy. We chose Zinc Hydroxide as an analyte. The reason for choosing this analyte is that the E6 protein, which is responsible for cervical cancer, contains a Zn atom in its structure [55]. This investigation will lead to a pathway to separate the E6 protein from a solution optically. This method can also be used to separate other metal ions. We report for the first time the experimental results based on Zinc Hydroxide, which shows that we can tweeze other compound in addition to GNRs. This is another accomplishment of the current investigation.

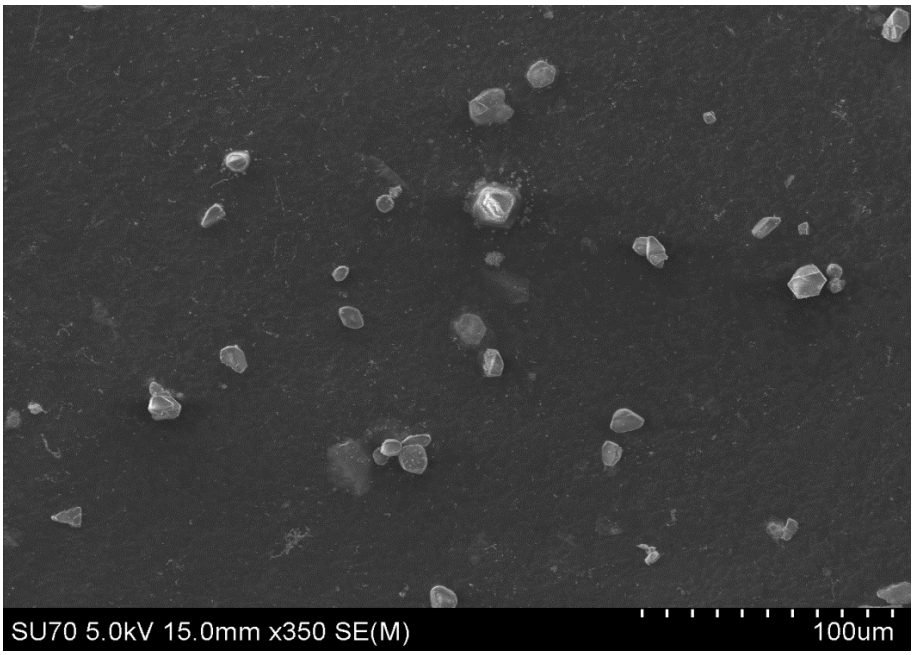

(a)

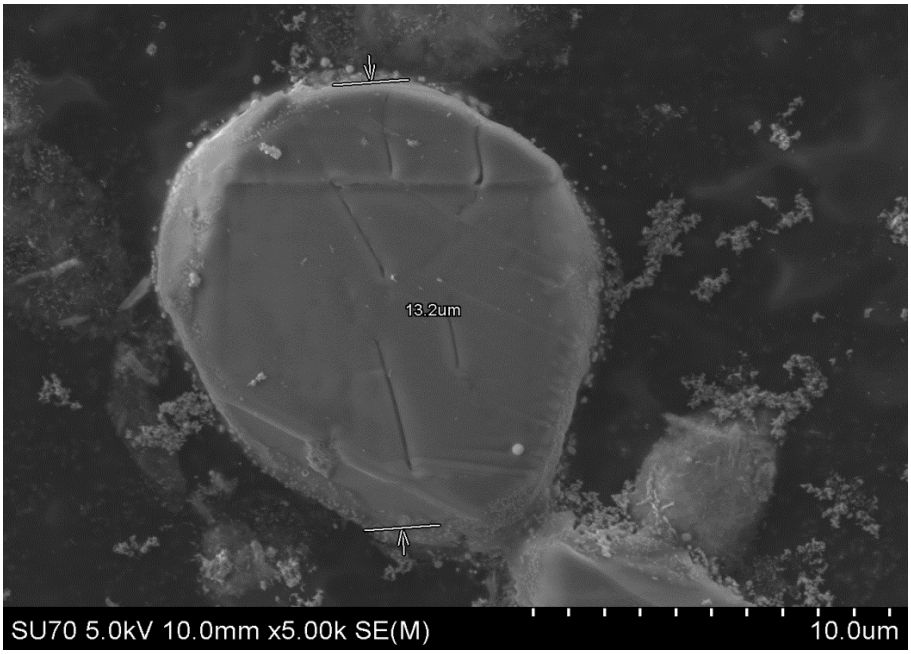

(b)

Figure 4.1: SEM images showing (a) the orthorhombic crystal shape and, (b) the magnified image indicating the orthorhombic shape of a single crystal of Zn $(OH)_2$.

To study the structure of Zn $(OH)_2$, one needs to examine the compound using SEM in a laboratory setting. In our experiment, 0.5 mg of Zinc Hydroxide (Zn $(OH)_2$) was mixed with 1000 µl of GNR solution. The concentration of the resulting solution was 0.5 µg/µl. A drop of the prepared solution was placed on the carbon tape of the SEM sample holder, and the solution was left to dry under a lamp for two hours. The sample holder was then placed in the SEM, and the voltage was set to 5 kV. The focus of the source of the electron beam was adjusted, and other alignments were done so that an electron beam could hit directly on the prepared sample.

Figure 4.1 (a) and (b) show the clear picture of the Zn $(OH)_2$ crystal. Further, the orthorhombic shape of the Zn $(OH)_2$ crystal is also visible. In Reference [56], a detailed study on schematic crystal structure of Zn $(OH)_2$ is given and we obtained the same results in figure 4.1

(b). Other morphology of Zn $(OH)_2$, such as a flower-like structure, was also seen in the experiment performed in addition to the orthorhombic shapes, as shown in Reference [57]. In addition, Figure 4.2 is based on Energy-Dispersive X-Ray Spectroscopy (EDS), which confirms the presence of Zinc and Oxygen in the Zn $(OH)_2$ compound. Hydrogen (H) is missing in the EDS results because the 1s level in H is not in the X-ray regime.

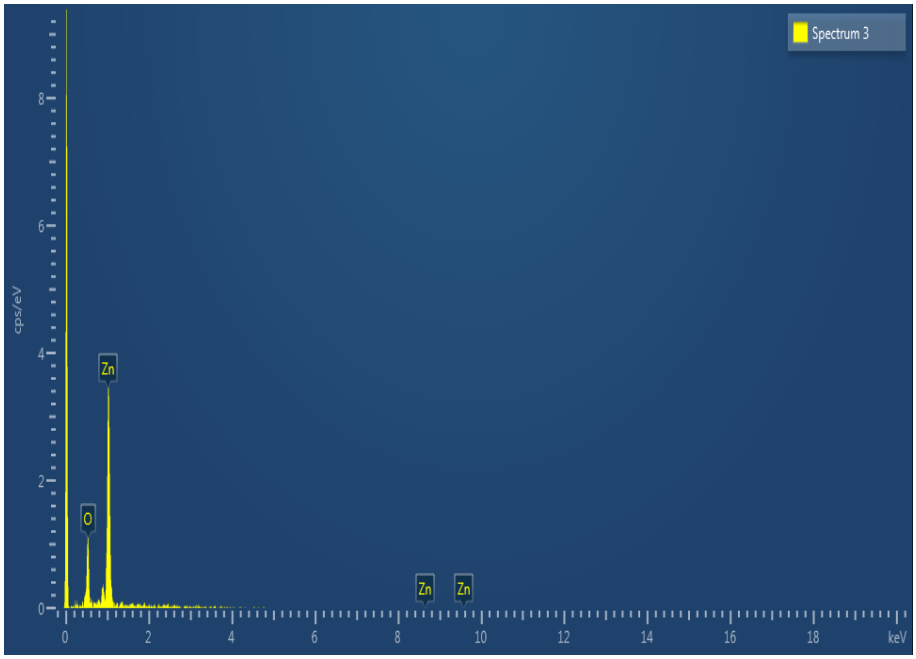

Figure 4.2: EDS results confirming the presence of Zinc corresponds to figure 4.1 (a) and (b), respectively.

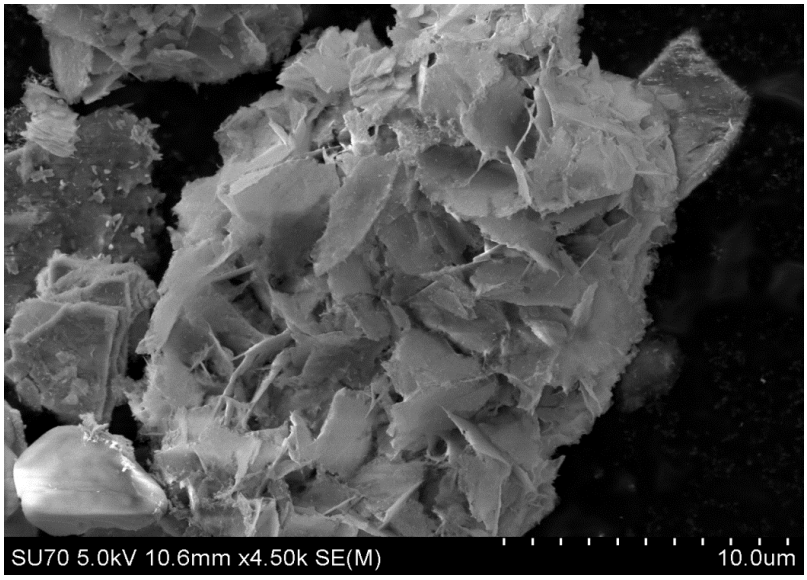

Figure 4.3: SEM image of Zn $(OH)_2$ showing the flower-like structure.

In Reference [56], the mechanism of deposition of ZnO and Zn $(OH)_2$ on activated carbon cloth by a chemical deposition method has been discussed. Additionally, different morphologies such as rhombic structures and flower-like structure of Zn $(OH)_2$ and ZnO, respectively are shown. Figure 4.3 was obtained when Zn $(OH)_2$ was mixed with GNR solution (0.4 μg/μl), and a drop of this solution was placed and scanned on the carbon tape of the SEM sample holder.

In this thesis, we reported for the first time the tweezing of a Zn compound on a tapered fiber probe. We also reported the SEM images and EDS spectrum to show the presence of Zinc Hydroxide on the surface of the tapered fiber along with GNRs. The experiments were performed using single and double tweezing, as described in Chapter 2. In the case of single tweezing (1064 nm), when tapered fiber was tweezed with Zn $(OH)_2$ and GNRs solution (conc. = 0.4 μg/μl), only GNRs were observed on the tapered fiber surface. We then performed double tweezing with two different lasers, where 0.4 μg/μl concentration, Zinc Hydroxide and GNR

solution was tweezed with two different laser wavelengths, i.e. 1064 nm (8.5 mW) and 632 nm (3.5 mW), consecutively. Flake-like structures of Zn $(OH)_2$ were seen at a diameter of 23.0 µm of the tapered optical fiber, as shown in figure 4.4.

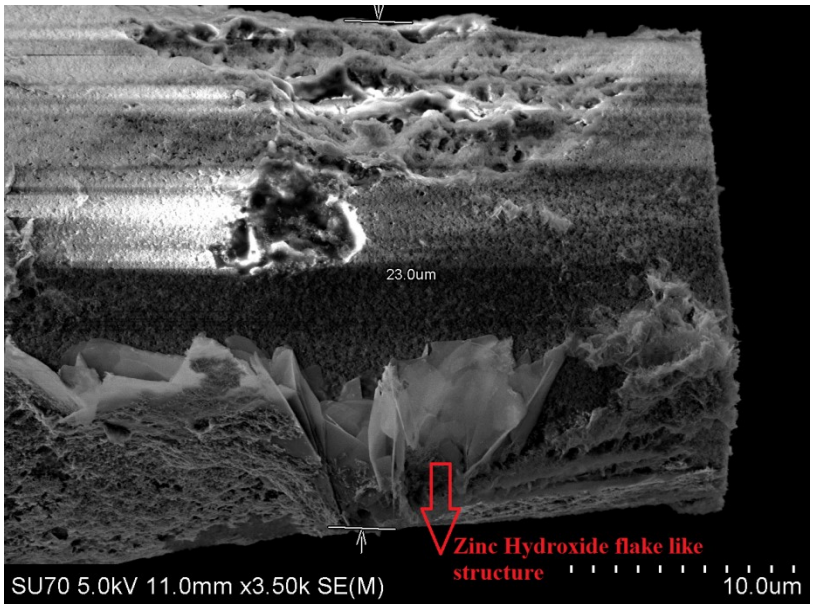

Figure 4.4: SEM image showing the presence of Zinc Hydroxide flower-like structure on the fiber surface when tweezed along with GNR solution with 1064 nm and 632 nm laser, consecutively.

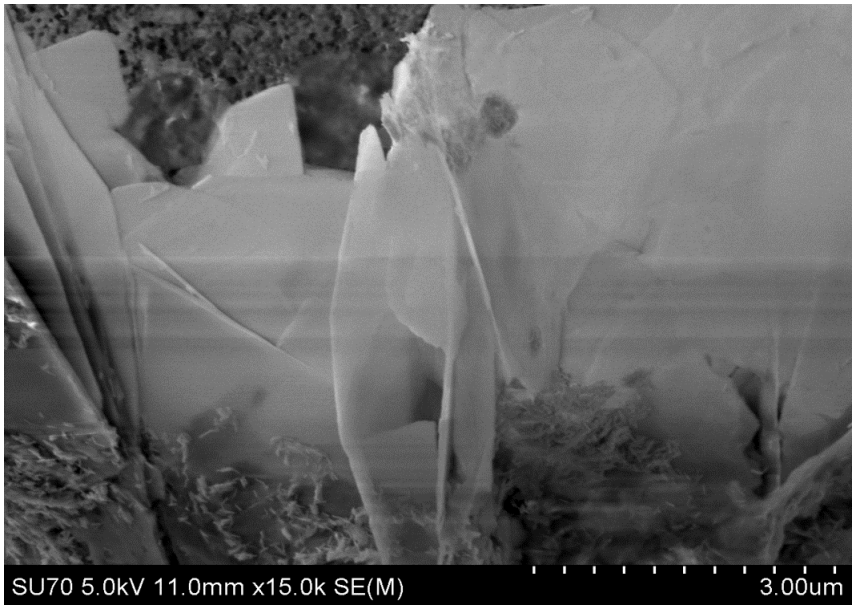

Figure 4.5: SEM image indicating the GNRs sitting on the flake-like structure of $Zn(OH)_2$ at 23 µm diameter (side view) of the tapered fiber after double tweezing.

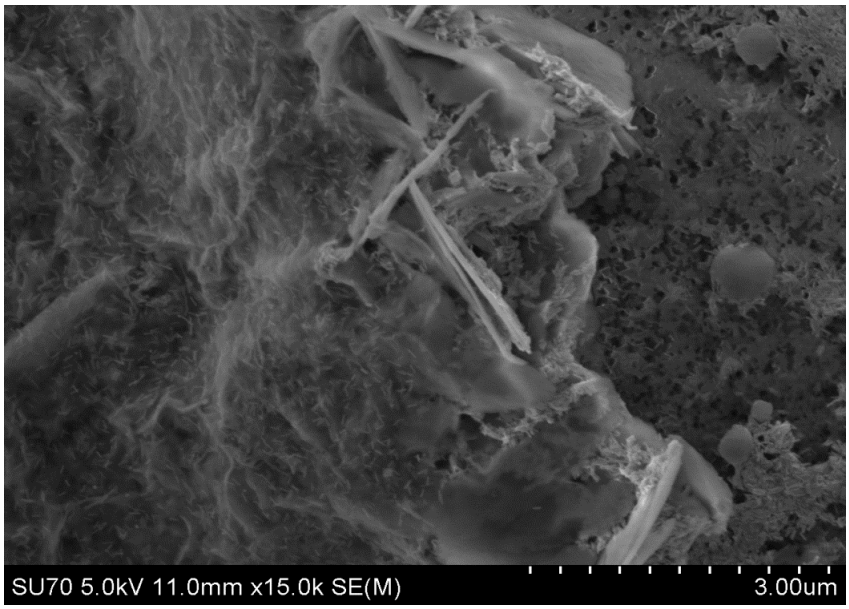

Figure 4.6: SEM image showing the flakes of Zn $(OH)_2$ with GNRs (top view).

Figure 4.5 shows an enlarged image (side view) of figure 4.4, where it shows flake-like structures that have arranged themselves in a flower shape along with the fiber with the GNRs. The top of this flower-like structure of Zn $(OH)_2$ along with GNRs is shown in figure 4.6, where it shows the alignment of Zn $(OH)_2$ flakes.

4.3 Conclusion and future work

In conclusion, the above experimental results show that we can tweeze a compound with Zinc ions once we mix it with GNRs. Also, different morphologies of Zn $(OH)_2$ were observed on the surface of the tapered fiber. It has been shown for the first time that Zinc Hydroxide can be tweezed on the fiber surface.

The next step is to tweeze different shaped and sized nanoparticles of Zn to explore the characteristic of the probe. Additionally, the optical tweezing of another metal ion such as lead etc. will also be a major focus in the future as it will be useful for the detection of contamination in water.

References

[1] **G. Keiser, *Optical Fiber Communications*, 3 ed. Boston, MA: McGraw Hill, 2000.**

[2] **K. C. Kao and G. A. Hockham, "Dielectric-fibre surface waveguides for optical frequencies,", 113 ed 1966, pp. 1151-1158.**

[3] **S. Addanki, I. S. Amiri, and P. Yupapin, "Review of optical fibers-introduction and applications in fiber lasers," *Results in Physics*, vol. 10, pp. 743-750, 2018.**

[4] **G. A. Valaskovic, M. Holton, and G. H. Morrison, "Parameter control, characterization, and optimization in the fabrication of optical fiber near-field probes," *Applied Optics*, vol. 34, no. 7, pp. 1215-1228, 1995.**

[5] **Y. K. Cheong, K. S. Lim, W. H. Lim, W. Y. Chong, and R. Zakaria, "Fabrication of tapered fibre tip using mechanical polishing method," *Review of Scientific Instruments*, vol. 82, pp. 086115-1-086115-3, 2011.**

[6] **H. Nikbakht, H. Latifi, M. Oraie, and T. Amini, "Fabrication of tapered tip fibers with a controllable cone angle using dynamical etching," *Journal of Lightwave Technology*, vol. 33, no. 23, pp. 4707-4711, 2015.**

[7] **J. O. Trevisanutto, A. Linhananta, and G. Das, "Plasmonic structure: fiber grating formed by gold nanorods on a tapered fiber," *Optics Lett.*, vol. 41, no. 24, pp. 5789-5792, 2016.**

[8] **Z. Chen, Z. Dai, N. Chen, S. Liu, F. Pang, B. Lu, and T. Want, "Gold nanoparticles-modified tapered fiber nanoprobe for remote SERS detection," *IEEE Phot. Tech. Lett.*, vol. 26, no. 8, pp. 777-780, 2014.**

[9] **Zeev Rosenzweig and Raoul Kopelman, "Analytical Properties and Sensor Size Effects of a Micrometer-Sized Optical Fiber Glucose Biosensor," *Analytical Chemistry*, vol. 68, pp. 1408-1413, 1996.**

[10] **S. Richard, "Second-harmonic generation in tapered optical fibers," *J. Opt. Soc. Am. B*, vol. 27, no. 8, pp. 1504-1512, 2010.**

[11] **Z. Liu, C. Guo, J. Yaug, and L. Yuan, "Tapered fiber optical tweezers for microscopic particle trapping: fabrication and application," *Optics Express*, vol. 14, no. 25, pp. 12510-12516, 2006.**

[12] **C. Viets and W. Hill, "Fibre-optic SERS sensors with conically etched tips," *Journal of Molecular Structure*, pp. 163-166, 2001.**

[13] **K. Sony and M. Soumya, "Preparation of Tapered Optical Fibers to utilize the Evanescent Field for Sensing Applications," *Internatinal Journal of Engineering Trends and technology*, vol. 4, no. 3, pp. 442-446, 2013.**

[14] **A. W. Snyder and J. D. Love, *Optical Waveguide Theory* Chapman and Hall Ltd, 1983.**

[15] **K. Karapetyan, W. Alt, and D. Meshchede, "Optical fibre toolbox for MATLAB, version 2.1, http://www.mathworks.com/matlabcentral/fileexchange/27819," 2011.**

[16] **A. Ashkin, J. M. Dziedzic, J. E. Bjorkholm, and S. Chu, "Observation of asingle-beam gradient force optical trap for dielectric particles," *Optics Letters*, vol. 11, pp. 288-290, 1986.**

[17] **A. Ashkin, "Trapping of Atoms by Resonance Radiation Pressure," *Physical Review Letters*, vol. 40, no. 12, pp. 729-732, 1978.**

[18] **A. Lehmuskero, P. Johansson, H. R. Dunlop, L. Tong, and M. Kall, "Laser Trrapping of Colloidal Metal Nanoparticles," *NANO*, vol. 9, no. 4, pp. 3453-3469, 2015.**

[19] **A. Ashkin, J. M. Dziedzic, and T. Yamane, "Optical trapping and manipulation of single cells using infrared laser beams," *Letters to Nature*, vol. 330, no. 24/31, pp. 769-771, 1987.**

[20] **S. Mondal, S. Pal, D. Kumbhakar, U. Tiwari, and R. Bhatnagar, "Evanescent wave assisted nanomaterial coating," *Applied Optics*, vol. 52, no. 22, pp. 5455-5459, 2013.**

[21] **C. Zhao, N. Chen, S. Liu, Z. Chen, and T. Wang, "Gold nanoparticles modified double-tapered fiber for SERS detection," *Journal of Physics: Conference Series*, vol. 844, pp. 1-5, 2017.**

[22] **K. C. Neuman and S. M. Block, "Optical Trapping," *Review of Scientific Instruments*, vol. 75, no. 9, pp. 2787-2809, 2004.**

[23] **K. Svoboda and S. M. Block, "Optical trapping of metallic Rayleigh particles," *Optics Letters*, vol. 19, no. 13, pp. 930-932, 1994.**

[24] **2. V. G. T. M. S. I. G. &. S. l. N. C. Aili Maimaiti1, "Higher order microfibre modes for dielectric particle trapping and propulsion,", 5 ed 2015, pp. 1-8.**

[25] **U. Kreibig and C. V. Fragstein, "The Limitation of Electron Mean Free Path in small silver particles," *Zeitschrift Fur Physik*, vol. 224, pp. 307-323, 1969.**

[26] **R. Narayanan and M. A. El-Sayed, "Catalysis with transition metal nanoparticles in colloidal solution: nanoparticle shape dependence and stability," *Journal of Physical Chemistry B*, vol. 109, no. 26, pp. 12663-12676, 2005.**

[27] **C. L. Haynes, A. J. Haes, A. D. McFarland, and R. P. Van Duyne, "Nanoparticles with tunable localized surface plasmon resonances," *Topics in Fluorescence Spectroscopy*, vol. 8, pp. 47-99, 2005.**

[28] **X. Lu, M. Rycenga, S. Skrabalak, B. Wiley, and Y. Xia, "Chemical synthesis of novel plasmonic nanoparticles," *Annual Review of Physical Chemistry*, vol. 60, pp. 167-192, 2009.**

[29] **M. Fleischmann, P. J. Hendra, and A. J. McQuillan, "RAMAN SPECTRA OF PYRIDINE ADSORBED AT A SILVER ELECTRODE," *Chemical Physics Letters*, vol. 26, no. 2, pp. 163-166, 1974.**

[30] D. L. JEANMAIRE and R. P. Van Duyne, "SURFACE RAMAN SPECTROELECTROCHEMISTRY PART I. HETEROCYCLIC, AROMATIC/ AND ALIPHATIC AMINES ADSORBED ON THE ANODIZED SILVER ELECTRODE," *J. ELECTROANAL CHEM.*, vol. 84, pp. 1-20, 1977.

[31] T. A. El-Brolossy, T. Abdallah, M. B. Mohamed, S. Abdallah, K. Easawi, S. Negm, and H. Talaat, "Shape and size dependence of the surface plasmon resonance of gold nanoparticles studied by photoacoustic technique," *European Physical Journal Special Topics*, vol. 153, pp. 361-364, 2008.

[32] P. Geshev, S. Klein, and M. Hietschold, "Calculation of the electric-field enhancement at nanoparticles of arbitrary shape in close proximity to a metallic surface," *Physical Review B*, vol. 70, pp. 075402-1-075402-16, 2004.

[33] X. H. Huang, S. Neretina, and M. A. El-Sayed, "Gold Nanorods: From Synthesis and Properties to Biological and Biomedical Applications," *Advanced Materials*, vol. 21, no. 48, pp. 4880-4910, Dec.2009.

[34] I. Ros, T. Placido, V. Amendola, C. Marinzi, N. Manfredi, R. Comparelli, M. Striccoli, A. Agostiano, A. Abbotto, D. Pedron, R. Pilot, and R. Bozio, "SERS properties of gold nanorods at resonance with molecular, transverse, and logitudinal plasmon excitations," *Plasmonics*, vol. 9, pp. 581-593, 2014.

[35] J. Cao, T. Sun, and K. T. V. Grattan, "Gold nanorod-based localized surface plasmon resonance biosensors: a review," *Sensors and Actuators B-Chemical*, vol. 195 2014.

[36] J. Perez-Juste, I. Pastoriza-Santos, L. Liz-Marzan, and P. Mulvaney, "Gold nanorods:synthesis, characterization and applicaiton," *Coordination Chemistry Reviews*, vol. 249, pp. 1870-1901, 2005.

[37] N. R. Jana, L. Gearheart, and C. J. Murphy, "Wet Chemical Synthesis of High Aspect Ratio Cylindrical Gold Nanorods," *J. Phys. Chem. B*, vol. 105, pp. 4065-4067, 2001.

[38] A. J. Haes and R. P. Van Duyne, "A highly sensitive and selective surface-enhanced nanobiosensor,", 723 ed 2002, p. O3.1.1-O3.1.6.

[39] G. Lu, T. Z. Forbes, and A. J. Haes, "SERS detection of uranyl using functionalized gold nanostars promoted by nanoparticle shape and size," *Analyst*, vol. 141, pp. 5137-5143, 2016.

[40] H. Feng, Y. Yang, Y. You, G. Li, J. Guo, T. Yu, Z. Shen, T. Wu, and B. Xing, "Simple and rapid synthesis of ultrathin gold nanowires, their self-assembly and application in surface-enhanced Raman scattering," *The Royal Society of Chemistry*, no. 15, pp. 5297-5305, 2009.

[41] Y. Sun and Y. Xia, "Increased Sensitivity of Surface Plasmon Resonance of Gold Nanoshells Compared to That of Gold Solid Colloids in Response to Environmental Changes," *American Chemical Society*, vol. 74, pp. 5297-5305, 2002.

[42] L. Lu, K. Ai, and Y. Ozaki, "Environmentally Friendly Synthesis of Highly Monodisphere Biocompatible Gold Nanoparticles with Urchin-like Shape," *American Chemical Society*, vol. 24, pp. 1058-1063, 2008.

[43] S. A. Ogundare and W. E. van Zyl, "A review of cellulose-based substrates for SERS: fundamentals, design principles, applications," *Cellulose*, vol. 26, pp. 6489-6528, 2019.

[44] L. M. Liz-Marzan, "Tailoring surface plasmons through the morphology and assembly of metal nanoparticles," *Langmuir*, vol. 22, no. 1, pp. 32-41, 2006.

[45] E. C. Le Ru, E. Blackie, M. Meyer, and P. G. Etchegoin, "Surface enhanced Raman scattering enhancement factors: a comprehensive study," *Journal of Physical Chemistry C*, vol. 111, no. 37, pp. 13794-13803, Sept.2007.

[46] S. Ben-Jaber, W. J. Peveler, R. Quesada-Cabrera, C. W.O.Sol, I. Papakonstantinou, and I. P. Parkin, "Sensitive and specific detection of explosives in solution and vapour by surface-enhanced Raman spectroscopy on silver nanocubes," *Royal Society of Chemistry*, vol. 9, pp. 16459-16466, 2017.

[47] D.-W. Li, W.-L. Zhai, Y.-T. Li, and Y.-Y. Long, "Recent progress in surface enhanced Raman spectroscopy for the detection of environmental pollutants," *Springer*, vol. 181, pp. 23-43, 2014.

[48] E. Scatena, S. Baiguera, and C. D. Gaudio, "Raman Spectroscopy and Aptamers for a Label-Free Approach: Diagnostic and Application Tools," *Journal of Healthcare Engineering*, pp. 1-11, 2019.

[49] A. Marques, B. Veigas, A. Araujo, B. Pagara, P. V. Baptista, H. Aguas, R. Martins, and E. Fortunato, "Paper-Based SERS Platform for One-Step Screening of Tetrecycline in Milk," *Nature*, vol. 9 2019.

[50] C. Liu, S. Wang, G. Chen, S. Xu, Q. Jia, J. Zhou, and W. Xu, "A Surface-enhanced Raman scattering (SERS)-active optical fiber sensor based on a three-dimensional sensing layer," *Sensing and Bio-sensing Research*, vol. 1, pp. 8-14, 2014.

[51] J. Wang, Y. Liu, Z. Li, G. Dong, J. Wang, and T. Liu, "A Reliable and Disp[osable Optical Fiber SERS Substrate," *Photonics and Electromagnetics Research Symposium*, pp. 3040-3045, 2019.

[52] N. K. Chen, K. Y. Lou, S. K. Liaw, W. H. Cheng, and R. Kashyap, "Fiber gratings formed by self-assembled nanoparticles," 2016.

[53] Y. W. Alsmeyer and R. L. McCreery, "Surface Enhanced Raman Examination of Carbon Electrodes: Effects of Laser Activation and Electrochemical Pretreatment," *American Chemical Society*, vol. 7, pp. 2370-2375, 1991.

[54] A. M. Michaels, M. Nirmal, and L. E. Brus, "Surface enhanced Raman spectroscopy of individual rhodamine 6G molecules on large Ag nanocrystals," *Journal of the American Chemical Society*, vol. 121, no. 43, pp. 9932-9939, 1999.

[55] K. Vaeteewoottacharn, S. Chamutpong, M. Ponglikitmongkol, and P. C. Angeletti, "Differential localization of HPV16 E6 splice products with E6-associated proteins," *Virology Journal*, 2005.

[56] M. Wang, Y. Zhou, Y. Zhang, S. H. Hahn, and E. J. kim, "From Zn(OH)2 to ZnO: a study on the mechanism of phase transformation,", 13 ed 2011, pp. 6024-6026.

[57] E. Mosayebi, S. Azizian, and A. Hajian, "Synthesis of nanostructured and microstructured ZnO and Zn(OH)2 on activated carbon cloth by hydrothermal and microwave-assisted chemical bath deposition methods,", 81 ed 2020, pp. 226-232.